Int J Earth Sci (Geol Rundsch) (2010) 99:1083–1110
DOI 10.1007/s00531-009-0447-z

ORIGINAL PAPER

Higher Himalayan Shear Zone, Zanskar Indian Himalaya: microstructural studies and extrusion mechanism by a combination of simple shear and channel flow

Soumyajit Mukherjee · H. A. Koyi

Received: 1 April 2009 / Accepted: 14 April 2009 / Published online: 21 May 2009

Abstract Thin-section studies of the Zanskar Shear Zone (ZSZ) rocks reveal a top-to-SW and subsequent primary and secondary top-to-NE ductile shearing; brittle–ductile and brittle extensions; top-to-SW brittle shear, steep normal faulting and fracturing. In the proposed two-phase model of ductile extrusion of the Higher Himalayan Shear Zone (HHSZ), a top-to-SW simple shearing during 22–18 Ma was followed by a combination of top-to-SW simple shear and channel flow at 18–16 Ma. The second phase simulates a thin ZSZ characterized by a top-to-NE shearing. The channel flow component ceased around 16 Ma, the extruding HHSZ entered the brittle regime but the top-to-SW shearing continued until perturbed by faults and fractures. Variation in the extrusion parameters led to variable thickness of the ZSZ. Shear strain after the extrusion is presumably maximum at the boundaries of the HHSZ and falls towards the base of the ZSZ, which crudely matches with the existing data. The other predictions: (1) spatially uniform shear strain after the first stage, (2) fastest extrusion rate at the base of the ZSZ, and (3) a lack of continuation of the ZSZ along the Himalayan trend are not possible to validate due to paucity of suitable data. Non-parabolic shear fabrics of the ZSZ indicate their heterogeneous deformation.

S. Mukherjee (✉)
Department of Earth Sciences, Indian Institute of Technology Bombay, Powai, Mumbai 400076, India
e-mail: msoumyajit@yahoo.com

H. A. Koyi
Hans Ramberg Tectonic Laboratory,
Uppsala University, 752 36 Uppsala, Sweden

Keywords Zanskar Shear Zone · Higher Himalayan Shear Zone · Extrusion · Ductile deformation · Channel flow model · Brittle deformation

Introduction

Intracontinental collision between the Indian- and the Eurasian plates since ~55 Ma had deformed and remobilized the Proterozoic Indian crust by dismembering it along a number of thrusts of regional dimensions viz. Main Central Thrust (MCT), Main Boundary Thrust, and Main Frontal Thrust (e.g. Gansser 1964; Thakur 1993; Valdiya 1998; Yin 2006). A part of this deformed crust presently occurs as a longitudinal strip as the 'Higher Himalaya' (Gansser 1964; Thakur 1993; Valdiya 1998) or 'Greater Himalayan Sequence' (Grujic et al. 1996, 2002), or 'Higher Himalayan Crystalline Sequence' (Vannay and Grasemann 2001; Vannay et al. 2004) with a cover of Tethyan Sedimentary Zone in the northeast and Lesser Himalayan sedimentary rocks in the southwest (Fig. 1a). From structural point of view, Higher Himalaya has been referred as the 'Higher Himalayan Shear Zone' (HHSZ) by the Roorkee school (Jain and Anand 1988; Jain and Manickavasagam 1993; Jain and Patel 1999; Manickavasagam et al. 1999; Jain et al. 2000, 2002, 2005; Mukherjee 2007; also Mukherjee and Koyi 2009a) and also as an 'orogenic channel' by the Dalhousie group (e.g., Beaumont et al. 2001, 2004; Jamieson et al. 2004).

The lowest boundary of the HHSZ is delimited by the MCT in the south that separates Lesser Himalayan rocks of greenschist facies to that of the Precambrian–Proterozoic amphibolite facies schistose and gneissose rocks of the HHSZ. The northern part of the HHSZ is characterized by profound magmatism, anatexis, migmatization, and

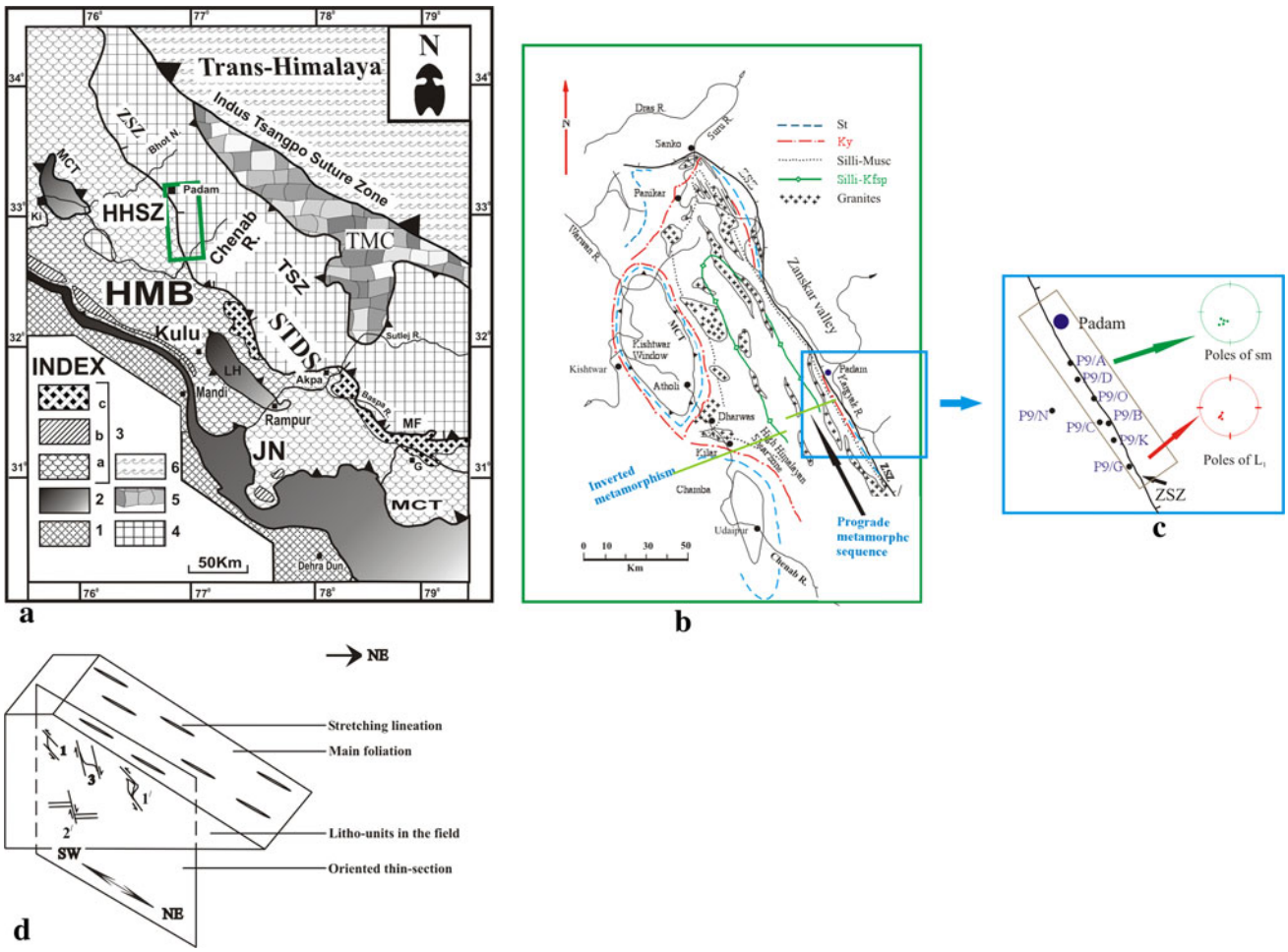

Fig. 1 **a** Simplified geological map of the NW Himalaya. Different Units: *1* Sub-Himalayan (SH) Cenozoic foreland basin, *2* Lesser Himalayan Sedimentary Zone (LHSZ), *3* Himalayan Metamorphic Belt (HMB): *a* Higher Himalayan Shear Zone (HHSZ) and Jutogh Nappe (JN) *b* ca. 500 Ma granitoid, *c* Cenozoic leucogranite. *4* Tethyan Sedimentary Zone (TSZ); *5* Tso Morari Crystalline (TMC) Belt; *6* Trans-Himalayan tectonic units. Tectonic boundaries: *MBT* Main Boundary Thrust, *MCT* Main Central Thrust, *STDS* South Tibetan Detachment System including Zanskar Shear Zone (ZSZ) and Martoli Fault (MF), *ITSZ* Indus Tsangpo Suture Zone. Locations: *Ki* Kishtwar, *S* Shimla, *UK* Uttarkashi and *G* Gangotri. From Jain et al. (2005). The *green box* shows the location of rocks on which microstructural studies are done in this work. The detail is shown in **c**. **b** Geological map of the Higher Himalayan Shear Zone in the Zanskar–Chamba–Kulu area, reproduced from Searle et al. (1988). Isograds are shown. Note that the term "High Himalaya" of Searle et al. (1988) is replaced here with the term "Higher Himalayan Shear Zone" of Jain and Anand (1988). The zones of inverted- and normal sequence of metamorphism are shown on the basis of disposition of staurolite-, kyanite-, sillimanite-muscovite and sillimanite-potassium felsdpar isograds. The studied thin-sections are from rocks within the ZSZ southeast to the place Padam. **c** Locations of rock samples southeast to Padam those were thin-sectioned and studied in this work. Poles of main foliations (S_m) and the stretching lineations (L_1) from the ZSZ, obtained from Figure 8h of Jain and Patel (1999), are plotted in respective stereograms. **d** A schematic cross-section of the Zanskar Shear Zone along the NE-SW geographic direction. The structures reported by Patel et al. (1993) are shown: *1* top-to-SW sense of ductile shearing, *3* top-to-NE (down) extensional ductile shearing, *1′* Top-to-SW sense of brittle shearing represented by duplexes, and *2′* Northeasterly steeply dipping brittle faulting. Ductile shearing represented by *1* and *3* are subsequently referred as 'shearing-1' and 'shearing-3', respectively. Primary shear planes of 'shearing-1' define the 'main foliations'. Stretching lineations plunge northeasterly. The orientation of the thin-sections, studied in this work, is perpendicular to the main foliations and parallel to the stretching lineations. The diagram is neither to scale nor angle

injection of granitic melt around 18 Ma (e.g., reviews by Searle 1999; Law et al. 2004; Vannay and Grasemann 2001; Jain et al. 2002; Yin 2006). The South Tibetan Detachment System (STDS) that separates Paleozoic Mesozoic Tethyan Sedimentary Zone in the north from the HHSZ in the south is a ductile normal shear zone with 15–18 km throw and 80 km heave (see review by Grujic et al. 1996) with local orogen parallel movement possibly of trivial regional significance (Yin 2006 and references therein). Compiled geochronologic data from different sectors of the Himalaya indicates that the ductile extensional shearing within the STDS and the ductile compressional shearing of the MCT

were active between 24–12 Ma and 25–14 Ma, respectively, with an overlapping period of activation between 24 and 12 Ma (Godin et al. 2006 and references therein). However, the period of (combined) activation of the STDS and the MCT varied from section to section in the Himalaya.

Compared to the different longitudinal tectonic units of the Himalaya, the HHSZ has received greatest attention amongst structural geologists due to its several unique geodynamic characters that were discovered in last few decades. These are (1) inverted metamorphism, (2) presence of extensional ductile shear zone in an overall compressional regime, (3) simultaneity of extensional ductile shearing within the top with the compressional shearing at its base around middle Miocene, and (4) presence of 3–7% partially molten crust in southern Tibet at a mid-crustal depth that partly acted as the source of extruded rocks of the HHSZ (see Godin et al. 2006; Yin 2006; Harris 2007 for reviews; Caldwell et al. 2009). Accordingly, four broad categories of models of extrusion vis-à-vis inverted metamorphism of the HHSZ have evolved since 1930s. These are (1) thermal-, (2) coupled thermo-mechanical-, (3) post-metamorphic deformation-, and (4) syn-metamorphic deformation models (Yin 2006). However, given a wide variation in tectonic framework of the HHSZ in different sections, none of the existing models could embrace all the extrusion constraints (see Hodges 2000 for review).

Recently channel flow model has evolved as an almost unanimously accepted extrusion mechanism of the wedge-shaped HHSZ in the Bhutan Himalaya (Grujic et al. 1996, 2002), implicitly that in the Zanskar section (Stephenson et al. 2001), and eventually for all the sections of the HHSZ as a general model by the Dalhousie research group (Beaumont et al. 2001, 2004; Jamieson et al. 2002, 2004). The Dalhousie school of modelers tuned the channel flow to initiate at 34 Ma at a mid-crustal depth of 25–30 km in a sub-horizontal channel below the over-thickened Tibetan plateau. The HHSZ acted as a linked inclined channel through which rocks extruded at the surface since around 24 Ma in different Himalayan sections (Harris 2007 and references therein). The channel flow extrusion has also been considered as the trigger of the out-of-sequence thrusting in the HHSZ in different sections (see Hollister and Grujic 2006; Carosi et al. 2007; Mukherjee 2007; Mukherjee et al. 2009).

We note a lack of strict terminologies in fluid mechanics to categorize specific flow patterns. For example, Rogers (1978) used the term 'plane Couette flow' to represent the 'Couette Poiseuille flow' of Schlichting (1955). In this work, 'channel flow'/'Poiseuille flow' will be used to denote laminar flow of an incompressible Newtonian viscous fluid under a pressure gradient through static parallel infinitely long walls of a channel. On other hand, the term 'combined simple shear and channel flow' will be used to denote a laminar flow under a pressure gradient and shearing of the walls. In the present study, we demonstrate after adding a few more tectonic constraints that a purely channel flow model is insufficient to describe the extrusion mechanism of the Zanskar section of the HHSZ in western Indian Himalaya. This paper aims at (1) micro-structural documentation of dominant deformation phases of the ZSZ rocks, (2) compilation of tectonic constraints of extrusion of the HHSZ, and (3) proposing a flow model of extrusion of the HHSZ, Zanskar section. The brittle–ductile and brittle deformations of the HHSZ reported here do not contribute to the proposed model but gives a complete picture of the deformation pattern and aftereffects of the ductile extrusion. Micro-structural studies of the HHSZ in this section have previously been pursued by Searle et al. (1992) but were restricted to work out prophyroblast-matrix relative time relationship from schistose rocks.

The study area

Geology

The Zanskar section of the HHSZ (Fig. 1b) in the Suru Doda valleys in Kashmir Indian Himalaya comprises of gneisses and schists, metapelites, metapsammites, calc-pelites, marble, amphibolite, mylonites, leucogranites, granitoids, aplites, pegmatites, and migmatites with greenschist to amphibolite facies metamorphism. The schists and the gneisses consist of sillimanite, kyanite, muscovite, and K-felsdpar. These rocks are Precambrian and Proterozoic in age and were intruded by leucogranites of Miocene Period (Patel et al. 1993; Dèzes et al. 1999; Jain and Patel 1999; Walker et al. 1999, 2001; Stephenson et al. 2001; Jain et al. 2002, 2005; Godin et al. 2006; Yin 2006). The STDS has been recognized in this section as the Zanskar Shear Zone (ZSZ) (Herren 1987; Patel et al. 1993; Dèzes et al. 1999; Jain and Patel 1999; Jain et al. 2002; Yin 2006). From the MCT towards the down dip direction of foliation planes in the northeast, the following isograds have been delineated:staurolite–garnet–biotite, kyanite and sillimanite–muscovite indicating an inverted metamorphic sequence. Further northeastward up to the ZSZ, this is followed by a normal sequence of metamorphism (Searle et al. 1988, as shown in Fig. 1b). In the Zanskar section of the HHSZ, a Barrovian M_1 metamorphism resulting from India to Asia collision followed by a lower pressure 21.5–19.5 Ma M_2 event coeval with anatexis in the upper part of the shear zone has been established (see review by Walker et al. 2001). Almost contemporaneous with the M_2-phase was extrusion of the HHSZ recorded by pronounced retrograde metamorphism in the ZSZ (Steck and Epard 2004).

Structures and tectonic constraints

Three phases of ductile deformation of the HHSZ in the Zanskar section were identified in field studies by Patel et al. (1993) and Jain and Patel (1999). Amongst these, a top-to-SW sense of ductile shearing along ~30° NE dipping primary shear planes (C-planes of Patel et al. 1993 and Jain et al. 2002; S_2 or S_m of Jain and Patel 1999; Walker et al. 2001) throughout the HHSZ belongs to the D_2 deformation phase. Mukherjee (submitted) and Mukherjee and Koyi (2009b) recently documented this deformation phase in terms of parallelogram-shaped cross-cutting element minerals of the type 1 flanking microstructures. Two phases of folding took place before and after this shearing event as the pre Himalayan D_1- and post shearing D_3-phases, respectively, at local scales (Jain and Anand 1988, Jain et al. 2002). In the ZSZ, a top-to-NE sense of extensional ductile shearing was documented, which is more abundant than the top-to-SW sense (Patel et al. 1993; Dèzes et al. 1999; Jain et al. 2002; Yin 2006).

The oldest record of a top-to-SW sense of ductile shearing of the MCT in the Zanskar section was dated to be 22 Ma (Walker et al. 1999). Yin (2006) considered the youngest activation period of the MCT to be prior to the initiation of doming of the Lesser Himalayan Kishtwar Window inside the HHSZ at 6 Ma. This means that the D_2-phase of deformation in the Zanskar section is bracketed between 22 and 6 Ma. Amongst the available timings of extensional ductile shearing in the HHSZ in the Zanskar section deduced from geochronology, e.g., <18–16 Ma (Inger 1998), 23–20 Ma (Walker et al. 1999) and 22.2–19.8 Ma (Dèzes et al. 1999), Godin et al. (2006) qualified the data by Inger (1998) to be that of the STDS in the Zanskar section. Thus, the MCT alone was active from 22 to 18 Ma, and simultaneous activation of the MCT and the ZSZ took place at least between 18 and 16 Ma. In the ZSZ, stretching lineations (L_2 or L_m of Jain and Patel 1999) plunge 25–38° northeasterly. A set of ~40° NE dipping ductile shear fabrics cut across the C-planes of the D_2 deformation phase. The top-to-NE sense of ductile shearing, associated with these northeasterly dipping shear planes, is henceforth referred as the top-to-NE (down) shearing. A phase of brittle deformation is deciphered from duplexes with a top-to-SW sense of shear. A subsequent phase of brittle deformation is deciphered from normal faults that dip steeply ~60–85°, cut across the primary brittle shear fabrics (Patel et al. 1993, Jain and Patel 1999), which is seemingly a manifestation of the Sarchu Fault of Dèzes (1999) or the Tanso Fault of Steck and Epard (2004). The dominant structures of the ZSZ compiled above are represented in the schematic cross-section in Fig. 1d. Compilation of vorticity numbers (ratio between simple shear to pure shear) from different sections of the HHSZ reveals that the top-to-SW sense of ductile shearing in the HHSZ was dominantly simple shear with some component of pure shear towards the middle of the shear zone (Carosi et al. 2007). In other words, an extrusion model of the HHSZ should consider ductile shearing of the rocks dominantly parallel to the primary shear C-planes.

For a qualitative extrusion model of the HHSZ, the rates of extrusion of its boundaries and the ratio of thickness of the zones of compressional and extensional shearing should be taken into account. Due to the paucity of all such data from the Zanskar section alone, in this work we rely selectively on those available from other sections. A similar approach was adopted in proposing the 'general shear model' of extrusion of the HHSZ by Vannay and Grasemann (2001). In the Nepal Himalaya, the rate of slip of the MCT was 3–5 mm $year^{-1}$ (Yin 2006). The rate of ductile slip in the ZSZ was at least two times faster and ranged between 1.2 and 4.2 cm $year^{-1}$ (Dèzes et al. 1999). A similar order of rate of slip of 2 cm $year^{-1}$ is given for the STDS (Annen et al. 2006 and references therein). The combined activation of the boundaries of the HHSZ gave rise to fast extrusion of the HHSZ at an average rate of 5.0–8.8 mm $year^{-1}$ (Dèzes 1999) along with extensive anatexis, migmatization, and leucogranite injection in the upper part of the HHSZ including the ZSZ (Walker et al. 1999; Yin 2006 and references therein). Secondly, the thickness of the ZSZ is in the order of few kilometers (Walker et al. 1999), which is much thinner than the greatest reported thickness of the HHSZ of 50 km by Jain and Anand (1988). Moreover, the thickness of the ZSZ varies along its length e.g., 2.25–6.7 km (Herren 1987), 0.5–2.5 km (Jain and Patel 1999), 1.6 km in average (Fig. 17 of Searle et al. 1988), 1 km (Dèzes 1999) in different outcrops. In the adjacent upper Kamirup valley, the thickness is only a few hundred meters (Steck and Epard 2004). On larger scales as well, the thickness of the continuation of the ZSZ along the trend of the Himalaya is spatially variable (Vannay and Grasemann 2001). For example, it is 5.2–7.3 km in the Sutlej section (Mukherjee and Koyi 2009a), at least 5 km in eastern Himalaya (Carosi et al. 1999), 1.5 km in the Dhaulagiri area in Nepal Himalaya (Kellet 2006; Kellet and Godin 2009), 1 km in the eastern Himalaya (Molli, Internet Reference) and especially in the Dzakaa Chu section (Cottle et al. 2007), and is as low as 350–400 m in the Annapurna section (Searle and Godin 2003).

The mid-crustal rocks of the over-thickened southern Tibet, at 25–30 km depth, have been inferred to be in a hot partially molten stage (Nelson et al. 1996). Recent magnetotelluric investigations from Garhwal sector of the Himalaya indicate the presence of a zone of low resistivity (<10 Ωm) around 5 km below the MCT zone possibly indicating partially melting (Israil et al. 2008). These evidences, along with the presence of migmatites in the upper

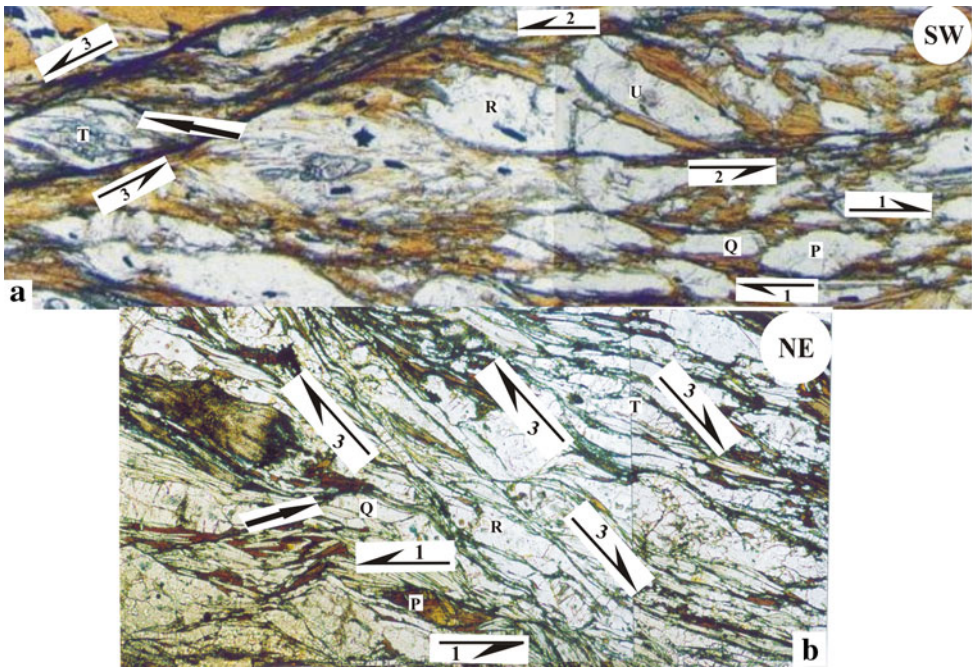

Fig. 2 **a** Intensely ductile sheared gneissose rock showing early top-to-SW sense of ductile shearing (marked by *half arrow 1*, henceforth referred as 'shearing-1'), and late and strong top-to-NE sense of ductile shearing (marked by *half arrow 2*, henceforth referred as 'shearing-2'). 'Shearing-1' occurs as relict. Its S-fabrics are defined by quartz grains, some of which are sigmoid shaped (grain *P*), and some are at very low-angle to the primary shear plane (grain *Q*). The long axes of these grains are at angle $\sim 7°$ to the shear plane *1*. Short and straight C-planes, bounding these quartz grains, are defined by biotite grains. Sigmoid and single-mouth quartz grains (*R* and *U*) define the S-planes for 'shearing-2'. The long axes of these grains are at angles 12° and 30°, respectively, to the shear plane *2*. The C-planes for the 'shearing-2' are parallel to, and therefore are the same as that for the 'shearing-1'. These C-planes are cut by prominent and thick C-planes of the top-to-NE (down) or 'shearing-3' at $\theta = 25°$. A sigmoid mineral fish of composite nature i.e., muscovite surrounding the staurolite core, aggregate *T*, defines its S-fabric. The long axis of *T* is at an angle 32° to the shear plane *3*. Aspect ratios of grains *P*, *Q*, *R*, *U* and the aggregate *T* are 2.9, 3.9, 3.0, 4.2, and 3.7, respectively. Photo in plane polarized light. XZ oriented thin-section from Zanskar Shear Zone. Photo length: 10 mm. Thin-section number: P9/A. **b** Recrystallized quartz grains (*R* and *T*) revealing top-to-NE (down) extensional shearing ('shearing-3' of caption of **a**). Relict top-to-SW ductile shearing ('shearing-1' in caption of **a**) is deciphered from a sigmoid fish defined by an aggregate of biotite (grain *P*), and a quartz fish (grain *Q*, pointed out by an *arrow*). Both these fishes have an aspect ratio of 4.8. The long axis of the quartz fish makes an angle of 7° to the shear plane *1*. This angle for the biotite fish is 11°. θ (defined in caption of **a**) is measured as 41°. Photo in plane polarized light. XZ oriented thin-section from Zanskar Shear Zone. Photo length: 4.0 mm. Thin-section number: P9/D

parts of the HHSZ suggest that in its ductile regime, the shear zone extruded like a fluid. A high rate of erosion of 0.53 ± 0.13 mm year^{-1} in this section of the HHSZ (Yin 2006 and references therein) might have augmented the extrusion process. The fact that erosion merely accelerated but did not modify the combined Couette- and Poiseuille flow of an extruding salt diapir of Newtonian rheology (Weinberger et al. 2006) supports the role of erosion in extrusion by similar mechanisms to be passive whether or not it is vigorous.

Micro-structural studies of the ZSZ

Studies of ductile deformation

Thin-section of sheared rocks from the ZSZ, southeast to the locality Padam (Fig. 1c), oriented perpendicular to the northeasterly dipping C-planes, or the 'main foliations' of the D_2 deformation, and parallel to the northeasterly plunging stretching lineations, were studied (Fig. 1d). The top-to-NE (down) shearing, also referred as 'shearing-3' in the text and figure captions, that cut the preexisting shear fabrics is found to be the most prominent deformation event, and is revealed by mineral fish (ten Grotenhuis et al. 2002) defined by minerals of both high- (grain 'T' in Fig. 2a) and low-grades (Figs. 2b, 3a), elongated (recrystallized) quartz grains (grains 'R' and 'T' in Fig. 2b; Fig. 3b, d) defining S-fabrics (Bèrthe et al. 1979) and intrafolial folds (Ghosh 1993) of aggregates of quartz and staurolite (Fig. 4a). The intrafolial folds are representative of D_1 deformation phase of Walker et al. (2001). The angle between the S- and the C- fabrics is around 47°. The enveloping surfaces of the intrafolial folds define the shear planes. On XZ thin-section, the axial traces of these folds make high-angle $\sim 70°$ to the SW direction along the C-planes.

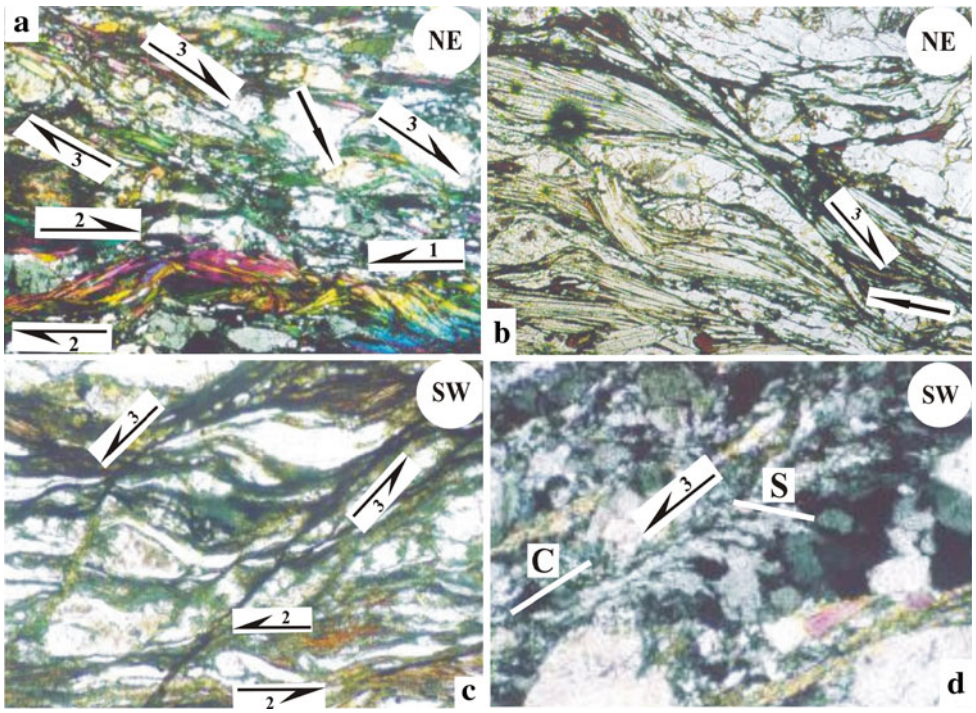

Fig. 3 **a** Intensely ductile sheared gneissose rock showing three senses of ductile shearing: top-to SW, top-to-NE, and top-to-NE (down), designated in the photograph as 'shearing-1', '-2' and '-3', respectively. The first two senses of shearing are represented by sigmoid fishes defined by an aggregate of muscovite grains. The last one is defined by individual micas defining the S-fabric, and also by sigmoidal quartz grains (pointed out by an *arrow*) that are partly wrapped by muscovite. θ (defined in caption of Fig. 2a) is measured as 40°. Photo in cross polarized light. XZ oriented thin-section from Zanskar Shear Zone. Photo length: 5.0 mm. Thin-section number: P9/O. **b** Top-to-NE (down) extensional shearing (same as 'shearing-3' of caption of Fig. 2a) has sheared recrystallized quartz grain into a long tail along the shear plane. This indicates that 'shearing-3' event has been pervasive. The shear plane is defined only at of the sides, shown by an *arrow* θ (defined in caption of Fig. 2a) measured elsewhere in the thin-section gives an amount of 53°. Photo in plane polarized light. XZ oriented thin-section from Zanskar Shear Zone. Photo length: 5.0 mm. Thin-section number: P9/B. **c** Sigmoid quartz grains of different thicknesses define the S-fabric and top-to-NE (down) extensional shearing (same as 'shearing-3' of caption of Fig. 2a) with decipherable thick and nearly straight C-planes. Top-to-NE sense of shearing ('shearing-2' of caption of Fig. 2a) is deciphered from intrafolial folds of quartz grains. θ (defined in caption of Fig. 2a) measured elsewhere in the thin-section gives an amount of 43°. Photo in plane polarized light. XZ oriented thin-section from Zanskar Shear Zone. Photo length: 5.0 mm. Thin-section number: P9/C. **d** Recrystallized quartz grains showing the S- and the C-fabrics. The S-fabric demonstrates top-to-NE (down) extensional shearing ('shearing-3' of caption of Fig. 2a). Interestingly, the S-fabric is defined, only at their contacts to the C-plane, by strongly swerved quartz grains. Instead of a pair of C-planes, a single C-plane is seen. Orientations of the S- and the C-planes are shown by *thin white lines*, and are at ~47°. θ (defined in caption of Fig. 2a) is measured as 36° elsewhere from the thin-section. Photo in cross polarized light. XZ oriented thin-section from Zanskar Shear Zone. Photo length: 5.0 mm. Thin-section number: P9/K

The second dominant deformation event is the top-to-NE sense of ductile shearing, 'shearing-2', typical of the STDS or of its continuation inferred to be active between 18 and 16 Ma. 'Shearing-2' is documented using sigmoid-shaped quartz fish (Figs. 2a, 4b, c) and intrafolial folds of aggregates of quartz (Fig. 3c) and that of recrystallized quartz (Fig. 4d). Quartz fish have been reported to be relatively rare in shear zones (Passchier and Trouw 2005), but are rather common in the ZSZ at micro-scale. Where overturned folding of a quartz vein is not sufficient to deduce the ductile shear sense (Fig. 5a), a preferred orientation of quartz grains (Vernon 2004) constituting such folds is used (Fig. 5b). Intrafolial folds of high-grade minerals are also used as a shear sense indicator (Fig. 6a). The axial traces of these folds in the oriented thin-sections are usually at low-angle, 13–21°, to the NE direction of the C-planes of the 'shearing-2' event (Figs. 5b, 6a). Besides, S-fabrics defined by preferred orientation and variation in sizes of quartz grains (Fig. 6b, c), and mica fish of different morphological varieties (Figs. 3a, 6d, 7a, b) are all indicative of this sense of shear. The angle between these S- and C-fabrics is around 30°.

A remnant top-to-SW sense of shearing, hereby denoted as 'shearing-1', is also documented, but such shear fabrics are less frequent and sometimes obscure. 'Shearing-1' is inferred to be the D_2 deformation phase of Jain et al. (2002) that persisted from 22 to 6 Ma, and is deciphered from different morphologies of mineral fish defined either by aggregates of mineral grains, also known as 'foliation fish' (Passchier and Trouw 2005) (grain 'T' in Fig. 2a; grain 'P'

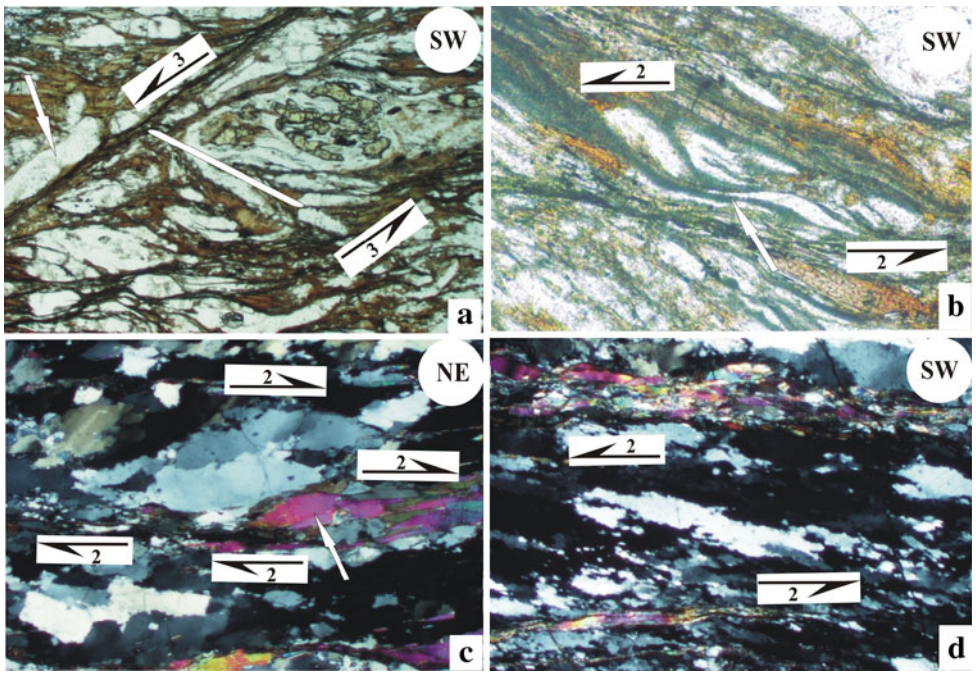

Fig. 4 **a** Broad hinge intrafolial fold defined by aggregate of quartz and staurtolite with markedly different limb thicknesses. The fold gives top-to-NE (down) extensional shearing ('shearing-3' of caption of Fig. 2a) along NE dipping thick and straight shear plane. The axial trace is marked by a *white line*. The shear plane is defined by elongated quartz grain, shown by an *arrow*. The angle between the axial trace and the C-plane of 'shearing-3' is 70°. Photo in plane polarized light. XZ oriented thin-section from Zanskar Shear Zone. Photo length: 3.0 mm. Thin-section number: P9/A. **b** Biotite aggregate and quartz grains strongly sheared in distinct zones into top-to-NE direction (the 'shearing-2' of caption of Fig. 2a) defining the S-fabric. The elongated corner of the quartz fish defines the shear plane, shown by an *arrow*. XZ oriented thin-section from Zanskar Shear Zone. Photo in plane polarized light. Photo length: 2.5 mm. Thin-section number: P9/D. **c**, **d** Top-to-NE shearing ('shearing-2' of caption of Fig. 2a.) are displayed by recrystallized quartz grains, which is a sigmoid shaped fish (**c**), or an overturned fold with unequal thicknesses- and lengths of the limbs (**d**). In **c**, the shear sense given by the quartz fish is confirmed by smaller muscovite fishes, shown by a *white arrow*. These fishes have aspect ratios 3.6 and 3.1, respectively. Their long axes make an angle ~15° to the 'shearing-2' plane. Photos in cross polarized light. For **d**, the angle between the S- and the C-planes is measured as 25°. XZ oriented thin-section from Zanskar Shear Zone. Photo length: 3.0 mm. Thin-section number: P9/G

in Fig. 2b, Fig. 6d) that are sigmoid-shaped, or by single minerals (Figs. 2a, b, 3a, 7a–d). Therefore, mineral fish in the studied thin-sections demonstrate both top-to-SW and top-to-NE senses of shearing. These two senses are also rarely observed adjacent to each other even in the single field of view under microscope (Fig. 7d).

Within the ZSZ, high-grade (Fig. 8a, b) and rigid (Fig. 8c) minerals have seldom been observed at high magnification to be hook-shaped. Wennberg (1996) demonstrated that on retro-shearing, the pro-sheared S-fabric keeps attaining lower angle to the C-plane opposite to its initial orientation and develops a hook (Fig. 8d). The specific orientation of these hooks with respect to the main foliation indicates unequivocally the sequence of ductile shearing. Hooks in the ZSZ are interpreted to have undergone a top-to-SW followed by a top-to-NE sense of retro-shearing. Such reactivation of more competent minerals such as quartz indicates that the retro-shearing in top-to-NE sense was quite intense. The sequence of ductile shearing in the ZSZ (Patel et al. 1993; Dèzes et al. 1999), in its continuation in the Bhutan Himalaya as the STDS (e.g., Grujic et al. 1996, 2002), and in the Pakistan Himalaya as the Main Mantle Thrust (Argles and Edwards 2002) was earlier deciphered from field studies solely on the basis of the abundance of top-to-NE fabrics over those showing a top-to-SW sense. In absence of the discovery of fabrics revealing a superposed shearing, however, this interpretation remained subjective. For example, an opposite sequence of ductile shearing, viz. from an early top-to-NE followed by a top-to-SW, was postulated from the Annapurna Shear Zone—a continuation of the ZSZ in the Nepal Himalaya (Godin et al. 1999). The prevailing view of first SW followed by a NE sense of shearing in the ZSZ is confirmed in the present micro-structural observations by the observed hook-fabrics with specific orientation to the C-planes.

The S-fabrics of 'shearing-1', '-2' and '-3' become progressively sigmoidally curved as they approach the shear planes. Mineral fish are the most ubiquitous indicators of ductile shear senses and are most often defined by micas.

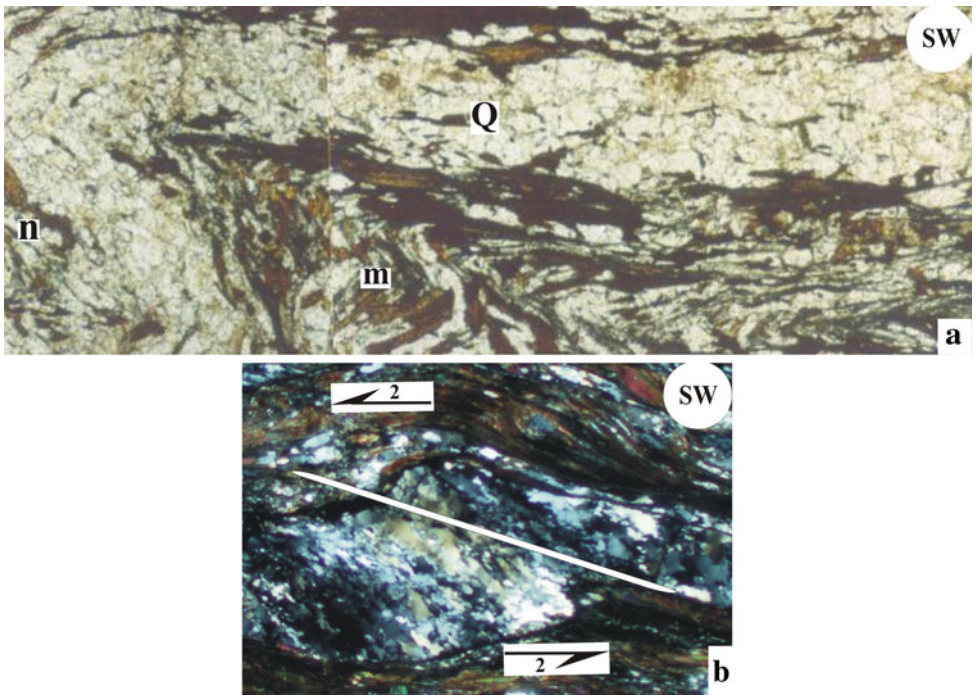

Fig. 5 **a** Overturned round hinge fold of Q-domain of quartz, shown by *Q*, with limbs of nearly equal thickness, and has southwesterly dipping axial plane. Thinner foliation planes, defined by alternate biotite- and quartz-rich layers, are tightly folded with sharp hinges and nearly straight limbs. These are located at both the sides of the folded Q-domain, and are shown by *m* and *n*. Since the 'enveloping surface' (Ghosh 1993) of this fold is not defined by straight foliation planes, the fold is probably not of intrafolial type. Therefore, no attempt is made to decipher the shear sense. Photo in plane polarized light. XZ oriented thin-section from Zanskar Shear Zone. Photo length: 2.0 mm. Thin-section number: P9/K. **b** Overturned fold of an aggregate of quartz grains. The sense of shearing deciphered from the fold vergence, and also from the shape preferred orientation of individual recrystallized grains, is ubiquitously top-to-NE ('shearing-2' of caption of Fig. 2a). The axial trace of the fold is marked by a *white line*. The angle between the axial trace and the C-plane of 'shearing-2' is 21°. Photo in cross polarized light. XZ oriented thin-section from Zanskar Shear Zone. Photo length: 3.0 mm. Thin-section number: P9/K

Mica fish shows a wide range of morphological variations e.g., mostly sigmoid (grain 'P' in Fig. 2b; Figs. 3a, 4b, 6d, 7a; grain 'n' in Fig. 7c, d), sometimes elliptical (grain 'n' in Fig. 7c) and rarely parallelogram-shaped (Fig. 7b), with usually no notches (grain 'P' in Fig. 2b; Figs. 3a, 4b, 6d, 7a, d), and infrequently two notches at its corners (grains 'm' and 'n' in Fig. 7c). Seldom the boundaries of the mica fish underwent dynamic recrystallisation (Fig. 7a, c), but usually they did not (grain 'P' in Fig. 2b; Figs. 3a, 4b, 6d, 7a). Dynamic recrystallisation at the boundary of the mica fish could be the reason for erosion of their corners and the genesis of notches (grain 'n' in Fig. 7c). Fine-grained minerals forming 'fish trails' at the corners of the mineral fish sometimes define the shear planes (Fig. 7a). Fish of different mineral species have aspect ratios (R = long axis/short axis) between 2 and 4.8, which is a rather narrower range than that previously reported as 2–16 from different shear zones by ten Grotenhuis et al. (2002). The angles between the long axes of the mineral fish to the ductile shear planes (the C-planes) fall within a broad range between 0 and 32°. Mineral fish with their long axes sub-parallel (<5°) to the C-plane were not used in shear sense determination (Fig. 7c).

With the documentation of 'shearing-2' and 'shearing-3' activated on the same mineral (Fig. 7a), or otherwise having an angular relation deciphered from distant positions in the thin-sections (Figs. 2a, b, 3a–d, 4a), the later is inferred to be a synthetic secondary (C′) shearing to the former. The C′-shear took place either simultaneous to, or later than, the C-shear event (Passchier and Trouw 2005). The C- and the C′-planes are characteristically long, prominent and straight (Figs. 2a, b, 3a–d, 4a), but are rarely undulating on the grain-scale (Fig. 6c). The remarkable straightness of the main foliations/C-planes has been considered as one of the constraints of extrusion of the Zanskar section of the HHSZ in the subsequent section. These shear planes are defined by (a) foliation minerals such as biotite (Fig. 2a); (b) elongated corners of sheared minerals (grain 'R' in Fig. 2b; Fig. 3b–d) and trails of minerals at the corners of mineral fish (Fig. 7a); and (c) grain size reduction (Fig. 6b, c). The ductile shear sense indicators are usually enveloped by a pair of shear planes (Figs. 2a, 3b, 4a, b, 6a–d, 7a). However, rare single shear planes were also encountered (Fig. 3b, d). The S-planes are defined either by single minerals such as 'mineral fish' (Figs. 2a,

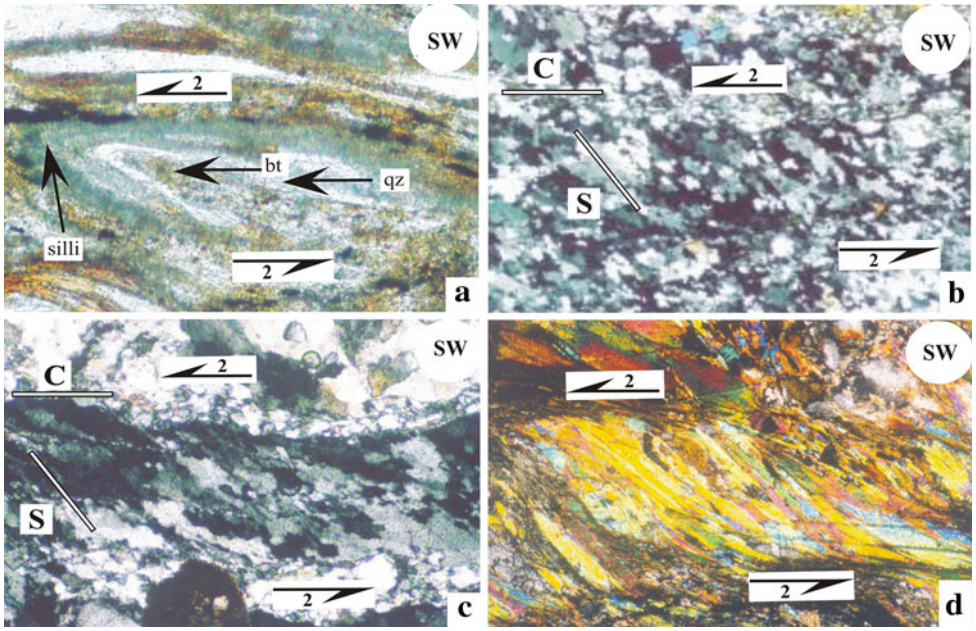

Fig. 6 **a** Rootless intrafolial fold of an aggregate of quartz (qz), biotite (bt) and sillimanite (silli) within gneissose rock giving a top-to-NE sense of shear ('shearing-2' of caption of Fig. 2a). The axial trace makes an angle of 13° with the primary shear plane. Photo in plane polarized light. XZ oriented thin-section from Zanskar Shear Zone. Photo length: 1 mm. Thin-section number: P9/N. **b**, **c** Recrystallized quartz grains showing S–C fabric indicating top-to-NE shearing ('shearing-2' of caption in Fig. 2a). The grains defining the C-planes are finer compared to those defining the S-planes. The C-plane is little undulatory in **c**, and is thicker than that in **b**. Orientations of the S- and the C-planes are shown by *thin white lines*, which are at 43° and ~44°, in **b** and **c**, respectively. XZ oriented thin-sections from Zanskar Shear Zone. Photos in cross polarized light. Photo length: 5.0 mm. Thin-section number: P9/D. **d** Top-to-NE extensional shearing ('shearing-2' of caption in Fig. 2a) indicated by sigmoidal foliation fish defined by a number of muscovite grains. The angle between the S- and the C-planes is 30°. Photo in cross polarized light. XZ oriented thin-section from Zanskar Shear Zone. Photo length: 5.0 mm. Thin-section number: P9/O

7a–d) or by the shape preferred orientation of an aggregate of minerals of otherwise anhedral shapes (Fig. 3d). The angles between the C and the C′planes measured in the XZ sections vary between 25 and 53°. This is a greater range than the 15–35° as previously compiled from different shear zones by Passchier and Trouw (2005). The secondary ductile shearing (C″) antithetic to 'shearing-2' is remarkably absent at micro-scale in the ZSZ.

Studies of brittle and brittle–ductile deformation

A top-to-SW sense of brittle shearing along 'Y' shear planes is interpreted from asymmetric duplexes defined by stacked-up of minerals of low- and high grades (Fig. 9a–c). These are identified by their morphological resemblance with different geometries of duplexes well established from field-scales (e.g., by McClay and Insley 1986 and references therein; Figures 6.93 and 6.96 of Davis and Reynolds 1996). To the knowledge of the authors, this is the first report of duplexes from the micro-scale. The thrust-up grains are typically hat- or trapezium-shaped with their straight boundaries unaffected by migration of the adjacent grains. The longest boundaries of these grains are identified as the 'P' shear planes of Passchier and Trouw (2005). The 'P' planes dip northeasterly at different angles, up to 35° to the Y-plane, and can be of variable curvature even within the same stack (Fig. 9c). The primary brittle shear planes, or the 'Y' planes (Passchier and Trouw 2005), bounding the micro-duplexes are traced in thin-section and are found to be continuations of C-planes for the 'shearing-1' or the 'shearing-2' events. In other words, the anisotropy created by the pre-existing ductile primary shear planes acted later as the preferential sites of brittle primary shearing. Nearly symmetric stacks of minerals (Figs. 9d, 10a) do not reveal any sense of shear. Symmetric duplexes in field-scale have been diagrammatically represented by Davis and Reynolds (1996). Nearly trapezium-shaped mica grains with straight grain boundaries and surrounded by quartzofeldspathic minerals may have their longest and straight boundaries sub-parallel to the Y-plane (Fig. 10b). These probably represent thrust slices that were transported relatively longer distances and became completely detached from the underthrust grains. Such grains were exempted from determination of brittle shear sense.

Few grains with irregular boundaries, even though overall hat-shaped (Fig. 10c, d), are actually the result of migration of adjacent grains into them (Figs 3.32 and 3.33 of Passchier and Trouw 2005) and are not produced due to

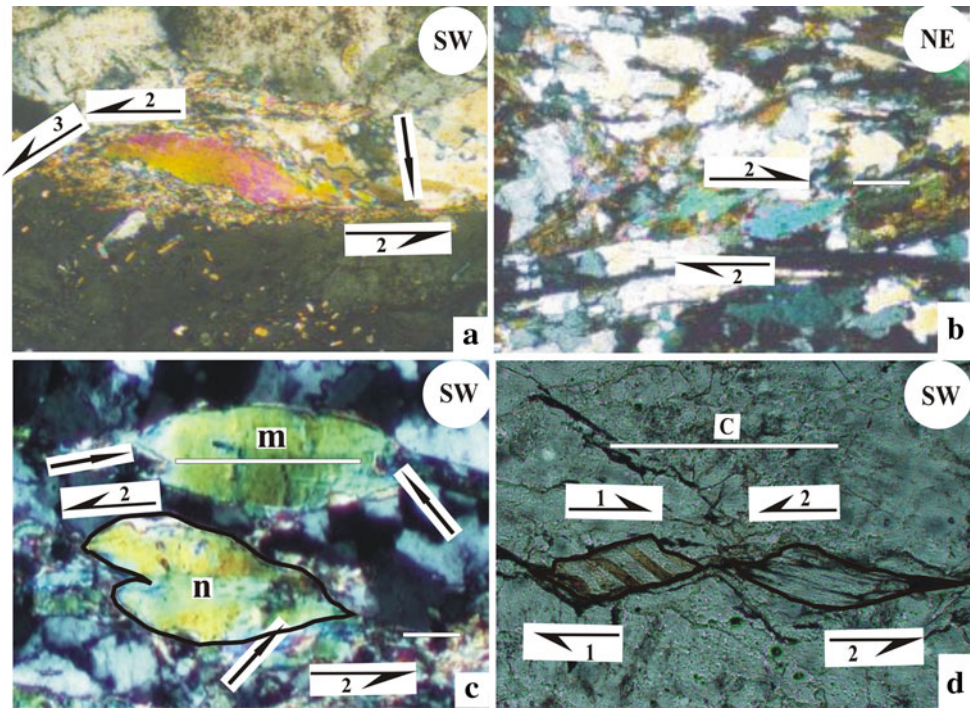

Fig. 7 **a** A sigmoid muscovite fish showing top-to-NE and top-to-NE (down) senses of shear- 'shearing-2' and 'shearing-3', respectively, defined in caption of Fig. 2a. Extensive dynamic recrystallization at the boundaries of the fish partly destructed its true shape. An *arrow* points to the fish trail that defines straight shear plane of 'shearing-2'. Neglecting recrystallization at its boundary, the aspect ratio of the fish is 4.4. The long axis of the fish makes 17° to the 'shearing-2' plane. The shear planes of the '-2' and '-3' events are at 30°. Photo in cross polarized light. XZ oriented thin-section from Zanskar Shear Zone. Photo length: 10 mm. Thin-section number: P9/B. **b** Two parallelogram-shaped muscovite fishes giving top-to-NE sense of shearing ('shearing-2' of caption in Fig. 2a). Dynamic recrystallization at the boundaries of the fishes has partly obliterated their accurate parallelogram shapes. The aspect ratios of these fishes at the left and at the right hand sides are calculated to be 2.8 and 3.5, respectively. The C-plane is shown by a *white line*. The long axes (same as the long diagonals here) of both these fishes make an angle of 14° to the 'shearing-2' plane. The acute angles between the 'shearing-2' plane and the sides of the parallelograms inclined at it are 26°. Photo in cross polarized light. XZ oriented thin-section from Zanskar Shear Zone. Photo length: 5.0 mm. Thin-section number: P9/G. **c** Grain *m*: a lenticular muscovite fish with mouths (notches) at both the sides. The orientation of the long axis of this grain is shown by a *white line*. The aspect ratio of this fish is 2. The main foliation (outside the photograph) is sub-parallel to the long axis of the grain. Therefore, this muscovite fish cannot be used to decipher the ductile shear sense. Grain *n*: a sigmoid shaped muscovite fish with a notch at one of its sides. The aspect ratio of this fish is 3 and its long axis is at 17° to the C-plane. The fish is partially destructed by extensive recrystallisation selectively at the lower left side where a notch is present, shown by an *arrow*. The sigmoid geometry of the fish shape is reconstructed with a *black line*. The C-plane is defined by trail of fine mica grains, shown by a *white line*. Photo in cross polarized light. XZ oriented thin-section from Zanskar Shear Zone. Photo length: 5.0 mm. Thin-section number: P9/C. **d** Two muscovite fishes within quartzofeldspathic matrix. The C-plane is deciphered outside the field of view of the photograph and is extrapolated on it as a *white line*. The asymmetry and inclination of these fishes with respect to the C-plane indicate 'shearing-1' and 'shearing-2' events. However, which shearing took place earlier could not be deciphered in this case. Photo in plane polarized light. XZ oriented thin-section from Zanskar Shear Zone. Photo length: 2.0 mm. Thin-section number: P9/A

thrusting. At micro-scale, the original rectangular shapes of the mica grains sometimes are modified by extensive migration of the neighbouring quartz grains into them and give rise to 'window structures' (Fig. 11) (Jessel 1987). In such cases of migration of one grain towards the other, the boundary of the 'intruding' grain in contact to the neighbour grain is convex towards the later. While deciphering duplexes of mica grains, therefore, the cases of micas with curvilinear contacts with the adjacent quartz grains were negated. In other words, trapezium-shaped grains with straight grain boundaries were only considered as thrust slices. A similar precaution was also adopted by Mukherjee (2007), (2008) and Mukherjee and Koyi (2009a) in sorting out trapezoidal grains from the HHSZ in other Himalayan sections.

The V-pull apart micro-structures of minerals (Hipperitt 1993) indicate a top-to-SW sense of brittle shearing (Fig. 12a–c), which supports those given by asymmetric duplexes. Both more competent- (Fig. 12a) and less competent minerals (Fig. 12c) underwent V-pull apart. The acute angles of the V openings are low and ranges between 10 and 27° for different minerals. The gaps created by the brittle separation of the clasts into the 'V' are filled in usually by chlorite and foliation planes in the matrix that get passive folded. The brittle deformation of the HHSZ has conventionally been idealized by the southward

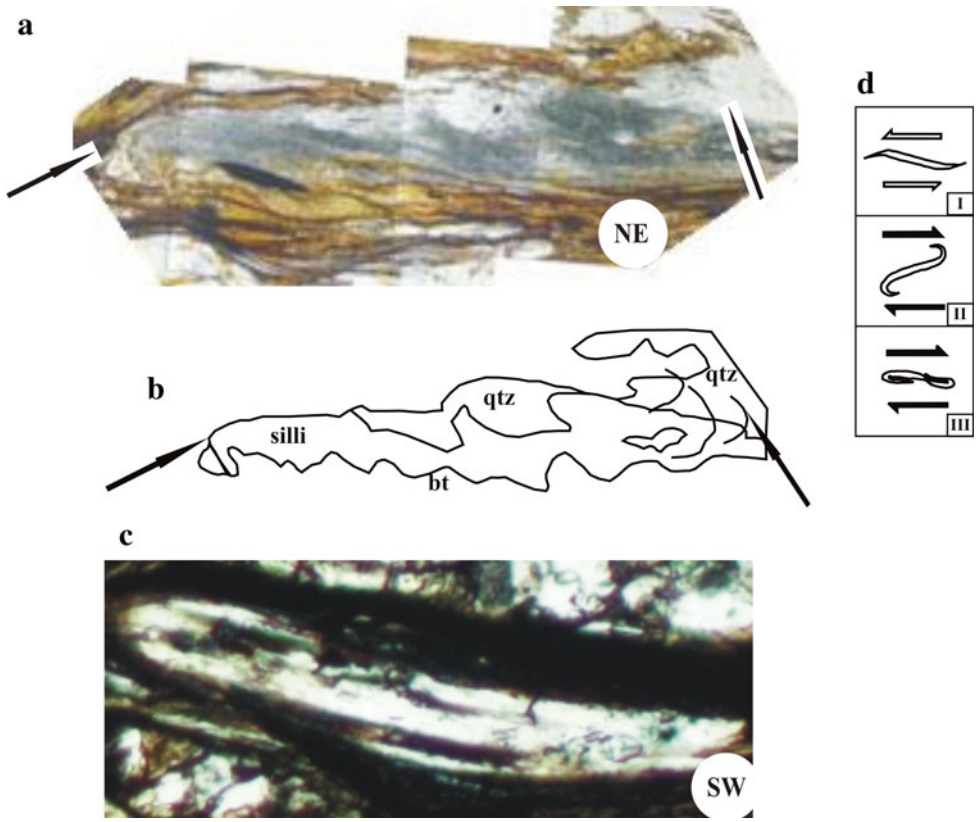

Fig. 8 **a** Dense intergrowth of sillimanite and biotite. Sillimanite occurs as fibrous and hazy aggregate, but its hook shape is still decipherable at the corners. The prominent curvatures of sillimanite, which define the hook, are pointed by *arrows*. The hook-shaped fabric is typically generated by reversal of ductile shear sense and is illustrated in **d**. A top-to-SW followed by a top-to-NE sense of shearing is deciphered. Photo in plane polarized light. XZ oriented thin-section from Zanskar Shear Zone. Photo length: 1.0 mm. Thin-section number: P9/N. **b** Line drawing sillimanite (silli) in **a**. Surrounding it are biotite (bt) and quartz (qtz). The prominent curvatures of sillimanite defining the hook geometry are pointed out by *arrows*. **c** Hook-shaped aggregate of quartz grains. An initial top-to-SW sense of shearing followed by a top-to-NE sense of retro-shearing, as shown in **d**, has given rise to the hook-shape. Photo in cross polarized light. XZ oriented thin-section from Zanskar Shear Zone. Photo length: 1.0 mm. Thin-section number: P9/B. **d** The fabric produced by the reversal of ductile shear sense is displayed: *I* An S-fabric produced by the top-to-left sense of shearing shown by *hollow half arrows*. *II* The fabric reactivates by a top-to-right sense of shearing, shown by *thick half arrows*. *III* Continuation of top-to-right sense of shearing orients the fabric at low-angle with the primary shear plane, and results in the hook shape. Reproduced from Wennberg (1996). The fabric in (*III*) and its orientation with respect to the shear plane is comparable with those of sillimanite- and quartz hooks in **a** and **c**, respectively

overriding of this shear zone as a single crustal block over the Lesser Himalayan rocks (Fig. 21 of Yin 2006). Contrary to this en-mass movement, the present micro-structural studies show that the top-to-SW sense of brittle deformation pervasively took place along pre-existing numerous discrete ductile shear planes, which therefore acted as the primary shear Y-planes of brittle deformation.

Brittle extension, parallel to the main foliation (the C-plane of 'shearing-1' and '-2', or the 'Y' plane), is deciphered by a number of parallel pull aparts (Hipperitt 1993) of originally single minerals (Fig. 12d). Such pull-aparts have a matrix of an aggregate of grains of smaller sizes. A set of grain boundaries of broken clasts are sub-parallel with each other and are nearly perpendicular to the main foliation planes. Brittle normal fault planes, north-easterly steeply dipping to $\geq 70°$, are deciphered by the abrupt offset of the individual minerals (Fig. 13a, b), and sometimes by the slip on the main foliation across them. These faults are identified as the secondary brittle shear planes, i.e., the R-planes of Passchier and Trouw (2005) that are synthetic to the 'Y' shearing event. The observed R-planes for the ZSZ are much steeper than their usual occurrence at $\sim 15°$ to the Y-planes as noted from other shear zones (Fig. 5.50 of Passchier and Trouw 2005). Along these R-planes, mineral grains underwent sharp slip but usually insignificant drag. In few cases, however, a lack of disrupted markers hindered recognition of the sense of slip (Fig. 13c). At micro-scale and within a single field of view, R-planes sometimes show significant variation in dip along their lengths (Fig. 13b). The R-planes are either remarkably straight (Fig. 13a) or are gently undulating (Fig. 13c). The gouge related to brittle faulting, and the

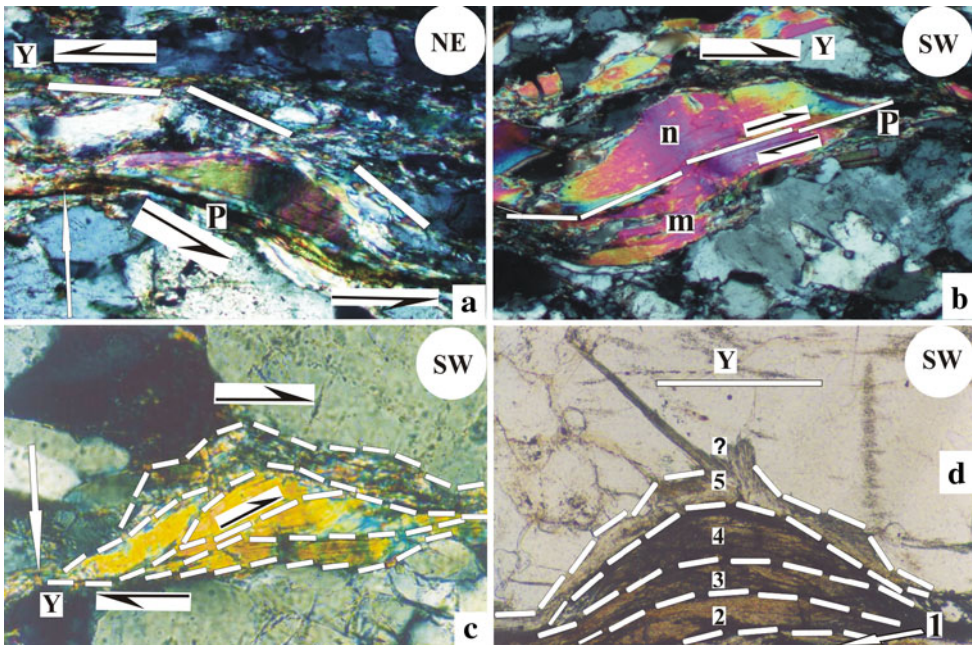

Fig. 9 **a** A muscovite grain is thrust over quartzofeldspathic grains, and gives a top-to-SW brittle sense of shear in the grain-scale. Note that the thrust-up muscovite grain is approximately trapezoid- or hat-shaped with nearly straight boundaries. Its longest boundary defines the thrust plane *P*, dips northeasterly at 25° to the Y-plane. Just above the muscovite hat, and below the *white lines* demarcated, the quartzofeldspathic minerals also take part in thrust movement as is revealed by concordance between their longest grain boundaries and the movement direction of the muscovite grain. Above the *white lines*, such concordance is not observed. The *Y* thrust plane delineating the lower boundary of the muscovite grain is pointed out by a *white arrow*. This plane is traced in the thin-section and is found to merge with the ductile shear plane of 'shearing-1' and '-2'. Photo in cross polarized light. XZ oriented thin-section from Zanskar Shear Zone. Photo length: 5 mm. Thin-section number: P9/D. **b** A hat-shaped muscovite grain *n* is thrust over another muscovite grain *m* in a top-to-SW sense in a brittle shear regime along the *Y* plane. The contact between these grains acts as the *P* shear plane, which dip northeasterly at angles 16° and 28° to the Y-plane. Grain *n* is nearly trapezoid-shaped. Photo in cross polarized light. XZ oriented thin-section from Zanskar Shear Zone. Photo length: 5 mm. Thin-section number: P9/G. **c** A number of asymmetrically stacked muscovite grains are demarcated by *broken white lines*. These are 'thrust slices' with grain to grain contact planes northeasterly dipping at variable angles, between 25 and 32°, and demonstrate a top-to-SW sense of brittle shearing. The brittle shear plane *Y* bounding the duplex, pointed out by a *white arrow*, is traced in the thin-section and is found to be the same as the ductile shear plane of 'shearing-1' and '-2'. Photo in cross polarized light. XZ oriented thin-section from Zanskar Shear Zone. Photo length: 2.5 mm. Thin-section number: P9/C. **d** Duplex structure defined by four staurolite grains (*1–4*) stacked one above another, and sillimanite (grain *5*) wraps the staurolite grain *4* at the top. Due to the overall symmetric shape of this antiformal stack, the brittle sense of shear cannot be deciphered. A part of the sillimanite grain projects like a long horn rendering question on its micro-structural significance. A *question mark* is placed where the horn originates. The *Y* plane is not defined in the field of view, but has been extrapolated as a *white line* from the other portion of the thin-section. Photo in cross polarized light. XZ oriented thin-section from Zanskar Shear Zone. Photo length: 2.5 mm. Thin-section number: P9N

antithetic secondary brittle shearing R′are expected to occur in shear zones even at micro-scale (Passchier and Trouw 2005), but are characteristically lacking in the ZSZ.

In these thin-sections, a set of T-fractures of Petit (1987) or 'transgranular fractures' of Fusseis and Handy (2008) are identified, which are at steep angles, 69°–86°, to the Y-planes (Fig. 14a, b). This range is narrower but is much higher than 20–50° as compiled from other shear zones by Passchier and Trouw (2005) and is nearly within the limit of 30°–80° as presented by Fusseis and Handy (2008). The fractures pervasively affected rigid minerals such as quartz. Some of these fractures refract while going from one layer into another even when these layers are constituted by the same mineral (Fig. 14a). The refraction at places has been so intense that the T-fractures alter their orientation from obtuse- to acute angle or vice versa along the Y-plane with respect to specific geographic direction ('arrow-1' in Fig. 14a, b). However, examples of insignificant refraction of the fracture planes do exist ('arrow-2' in Fig. 14a, b).

At higher magnifications, boudins of different varieties viz, pinch and swell structures (Fig. 15a), lenticular boudins (Fig. 15b, c), foliation boudins (Fig. 15d) and fish mouth lenticular boudins (not presented in this paper) are documented. Pinch and swell structures indicate insufficient tectonic force in comparison to the rigidity of these clasts to separate them into two completely separate pieces. On other hand, lenticular- and foliation boudins denote small competence contrast between the boudins and the matrix (Ghosh 1993). Single mineral (Fig. 15a–c) and also mineral aggregates constituting the main foliation

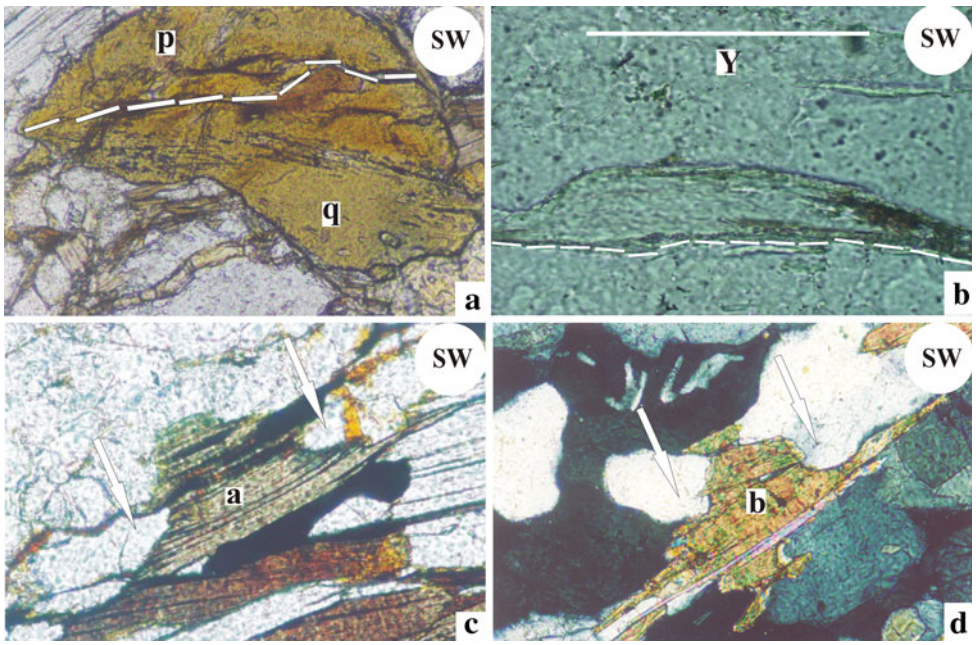

Fig. 10 **a** A staurolite grain *p* is stacked over another staurolite grain *q* defining a duplex. The boundary between them is marked by a *broken white line*. Weak asymmetry of antiformal shape of the overthrust grain *p* prevents to determine unambiguously the brittle sense of shear. Photo in plane polarized light. XZ oriented thin-section from Zanskar Shear Zone. Photo length: 5.0 mm. Thin-section number: P9/A. **b** A muscovite grain is surrounded by quartz grains. The muscovite looks like a thrust slice. The longest boundary of the grain is sub-parallel to the *Y*-plane. The *Y*-plane is deciphered from other places in the thin-section. The counterpart underthrust grain is outside the field of view. The grain might be overthrust and transported to a longer distance and crossed the underthrust grain. No attempt is made to find out the brittle sense of shearing from this, and such grain. Photo in plane polarized light. XZ oriented thin-section from Zanskar Shear Zone. Photo length: 5.0 mm. Thin-section number: P9/A. **c**, **d** Hat-shaped biotite grains, *a* and *b*, respectively, in the two photomicrographs. However, it is not a duplex since the shapes are products of migration of boundaries of adjacent quartz grains into them—pointed out by *arrows*. The quartz grains are convex towards the muscovite grains. Photos in plane- and in cross polarized lights, respectively. XZ oriented thin-section from Zanskar Shear Zone. Photo length: 5.0 mm. Thin-section number: P9/O

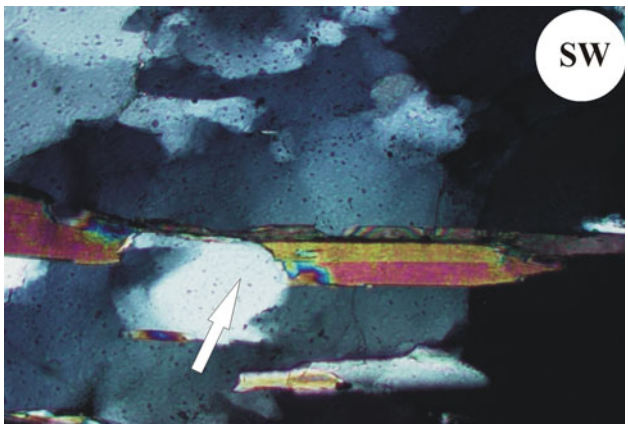

Fig. 11 The boundary of a quartz grain migrated and partially destructed the rectangular shape of a muscovite grain giving rise to a 'window-microstructure' of Jessel (1987), shown by an *arrow*. The quartz grain is convex towards the muscovite grain. Photo in cross polarized light. XZ oriented thin-section from Zanskar Shear Zone. Photo length: 2.5 mm. Thin-section number: P9/9

(Fig. 15d), are boudinaged. The aspect ratios (long axis/short axis) of the boudinaged clasts ranges between 3.3 and 4.3, which is narrower than 2–20 as compiled by Ghosh (1993) from different shear zones. In all the observed cases, the long axes of the boudinaged clasts are parallel to the main foliation. Variable distances amongst individual boudins of different shapes indicate variation in their rigidities and/or local brittle–ductile extension parallel to the main foliation at micro-scale. Rigid clasts such as quartz have been boudinaged even when they are present in quartzofeldspathic matrix of presumably similar competency (Fig. 15a–c). Similar cases of muscovite boudins within muscovite matrix were also documented (in collection with authors). These boudins are characterized by a lack of quartz veins between pairs of adjacent clasts. Microboudins have previously been reported often to be zoned by some other minerals (Passchier and Trouw 2005). However, such zones are lacking in the boudins in the ZSZ at micro-scale.

Structural compilation

The structural geology of the HHSZ relevant for the extrusion of the shear zone during 22–16 Ma is summarized in a NE–SW cross-section of the shear zone in the

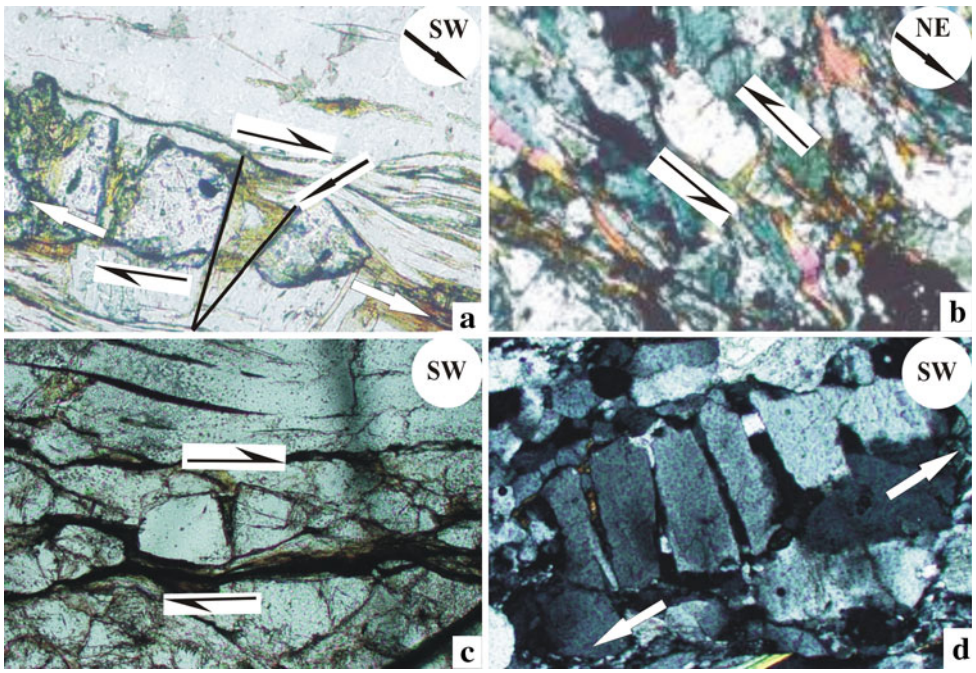

Fig. 12 **a** A V-pull apart of garnet with chlorite infilled at the V-opening and passive folded, pointed out by a *black arrow*. Note that just above the chlorite grain, a long muscovite grain is infolded within the V gap. The broken garnet grains are also away from each other along the main foliation, shown by a pair of *white arrows*. Sense of brittle shear is top-to-SW. The acute angle of the *V* is 26° and is calculated by extrapolating the matching boundaries of the garnet grain as *thick black lines*. Photo in plane polarized light. XZ oriented thin-section from Zanskar Shear Zone. Photo length: 5 mm. Thin-section number: P9/A. **b** A V-pull apart of alkali feldspar showing top-to-SW sense of brittle shearing. The acute angle of the *V* is 11°. Photo in cross polarized light. XZ oriented thin-section from Zanskar Shear Zone. Photo length: 10 mm. Thin-section number: P9/G. **c** A lenticular muscovite fish that got V-pull apart, demonstrates a top-to-SW sense of brittle shearing. The acute angle of the *V* is 21°. Photo in cross polarized light. XZ oriented thin-section from Zanskar Shear Zone. Photo length: 10 mm. Thin-section number: P9/K. **d** A set of parallel pull aparts of alkali feldspar grain. The direction of extension is shown by *white arrows* nearly parallel to the main foliation/C-plane of 'shearing-1' or 'shearing-2'. The main foliation is defined outside the photograph. Photo in cross polarized light. XZ oriented thin-section from Zanskar Shear Zone. Photo length: 2.5 mm. Thin-section number: P9/C

Zanskar section in Fig. 16. While the structures shown in the ZSZ are compiled from the present micro-scale study of ductile, brittle–ductile and brittle deformations, those in the remainder of the HHSZ were taken from Jain and Anand (1988) and Jain et al. (2002). The pre-Himalayan D_1 deformation phase older than the 22 Ma, superposed folding events of Patel et al. (1993) and the later D_3 phases of folding apparently younger than 6 Ma are characterized by deformations on a very local-scale in the HHSZ (Jain and Anand 1988, Jain et al. 2002).

Model for extrusion and ductile deformation

Formulation of the model

The following constraints are chosen to propose a model for extrusion in the ductile deformation regime of the HHSZ, Zanskar section.

(I) The main foliation/primary shear planes in the HHSZ including the ZSZ are N/NE dipping and are regionally planar.

(II) The top-to-SW sense of shearing throughout the HHSZ persisted during 22–18 Ma.

(III) The top-to-SW sense of ductile shearing within the ZSZ was followed by a top-to-NE sense of ductile shearing.

(IV) In the ZSZ, a top-to-NE sense of ductile shearing persisted during 18–16 Ma while a top-to-SW sense of ductile shearing of the MCT took place.

(V) The extrusion of the HHSZ took place dominantly under simple shear deformation.

(VI) From the MCT up to some distance within the HHSZ, inverted metamorphism persists. From this place towards north till the end of the ZSZ, a normal sequence of metamorphism is prevalent.

(VII) At least a part of the ductile extrusion of the HHSZ took place as a fluid.

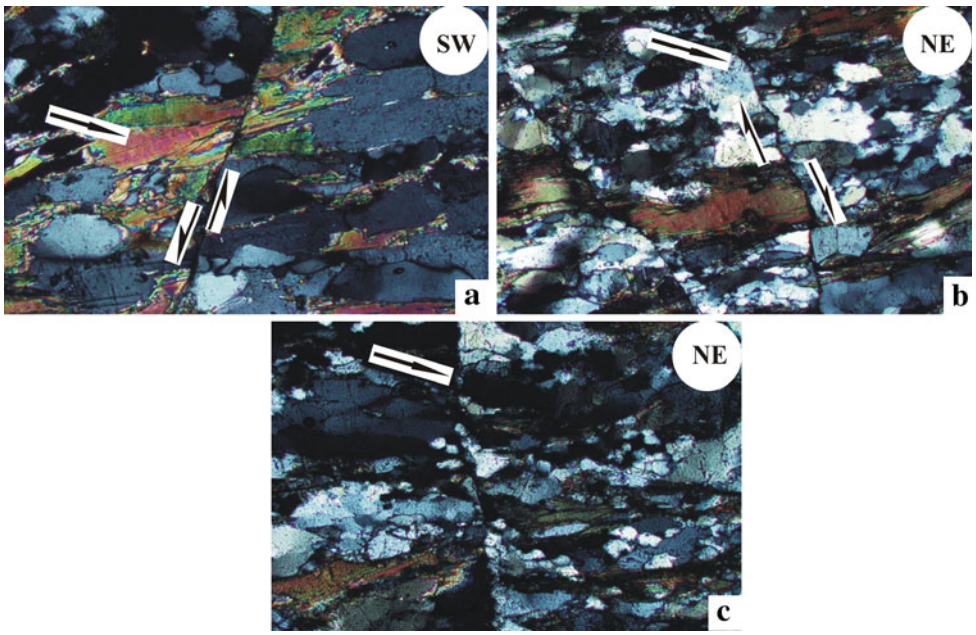

Fig. 13 **a** Sharp brittle normal fault, northeasterly steeply dipping and at 70° to the main foliation shows prominent slip and weak drag of the biotite aggregate across it. The faulted aggregate of biotite is pointed out by an *arrow* at one of the sides of the fault. Photo in cross polarized light. XZ oriented thin-sections from Zanskar Shear Zone. Photo lengths: 5 mm. Thin-section numbers: P9/D. **b** Sharp brittle normal fault cutting the main foliation at steep angle at ~90°. Prominent slip but no drag of a quartz grain across the fault is noted, pointed out by an *arrow* at one of the sides of the fault. Photo in cross polarized light. XZ oriented thin-sections from Zanskar Shear Zone. Photo length: 5 mm. Thin-section number: P9/B. **c** Sharp brittle normal fault, northeasterly steeply dipping, at 70° to the main foliation. Abrupt termination of grains across this fault is noted but no disrupted marker could be established thereby making it intangible whether the fault is normal or reverse. Photo in cross polarized light. XZ oriented thin-section from Zanskar Shear Zone. Photo length: 5 mm. Thin-section number: P9/K

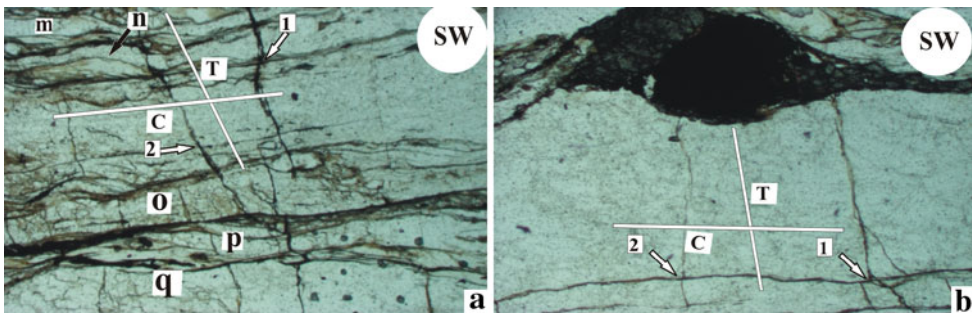

Fig. 14 **a** A number of quartz veins *m*, *n*, *o*, *p*, and *q* are cut by a set of sub-parallel T-fractures of Petit (1987). The veins are oriented sub-parallel to the *C*-plane. T-fractures are at high acute-angle to the *C*-plane in the SW direction. The orientation of the *C*-plane is shown by a *white line*. The angle between the *T*- and the *C*-planes, shown by *white lines*, is 69°. The T-fractures sometimes refract while crossing one layer into another, (*arrow 1*), though not always (*arrow 2*). Photo in plane polarized light. XZ oriented thin-section from Zanskar Shear Zone. Photo length: 5.0 mm. Thin-section number: P9/N. **b** In comparatively thicker layers of quartz, T-fracture planes are developed at steep angle ~77° to the quartz layers. Their average orientations are shown by a *white line*. The quartz layers are sub-parallel to the C-planes. The T-fractures are refracted while entering different layers of minerals (*arrow 1*), though not always (*arrow 2*). Photo in plane polarized light. XZ oriented thin-section from Zanskar Shear Zone. Photo length: 1 mm. Thin-section number: P9/O

(VIII) The ZSZ is thinner than the remainder of the HHSZ.

(IX) The thickness of the ZSZ varies along its length at local- and regional scales.

(X) The rate of extensional slip in the ZSZ was faster than that of the compressional slip of the MCT.

Constraint I and III–VII were utilized by Beaumont et al. (2001, 2004) and Jamieson et al. (2004) in proposing the classical channel flow extrusion model. The third constraint is confirmed from the present micro-structural studies. Constraints VIII–X are new additions in this work through compilation of previous literature.

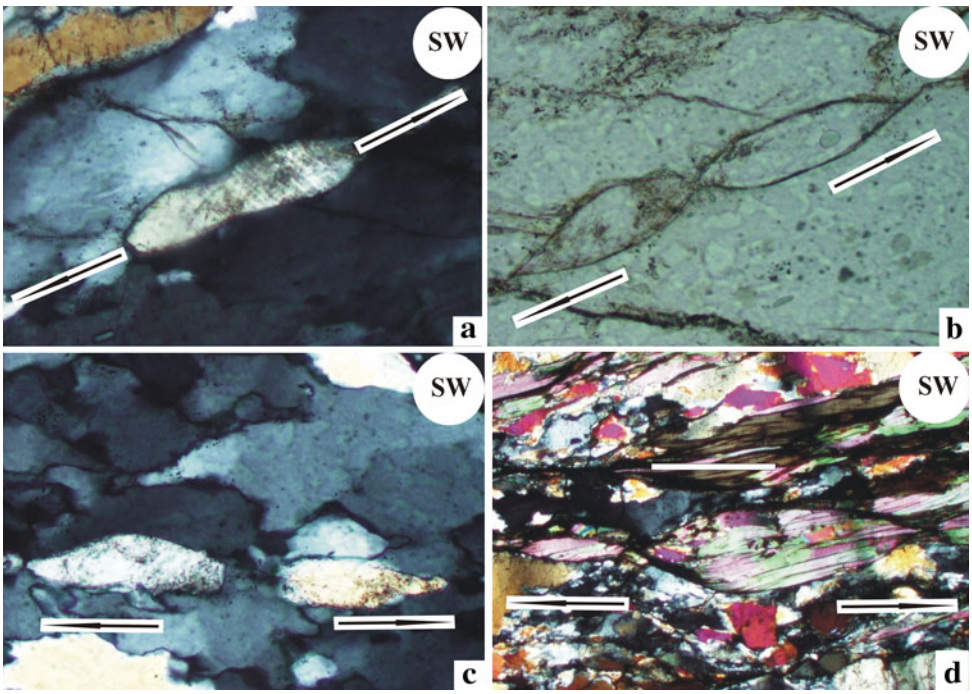

Fig. 15 Different geometric types of boudins. The direction of extension is shown by *arrows*, which are parallel to the main foliation/C-plane of 'shearing-1'. Note that the main foliation is not within the field of view in **a** and **b**. **a** Pinch and swell structure of alkali feldspar, indicating that the extensional force was not strong enough to separate the single clast into two completely separated pieces. Photo in cross polarized light. XZ oriented thin-section from Zanskar Shear Zone. Photo length: 0.5 mm. Thin-section number: P9/A. **b**, **c** Lenticular boudin of alkali feldspar. While in **b**, the individual clasts are in point contact, those in **c** are completely separated. The 'elongation' (Ghosh 1993) of the boudin in **c** is 0.15 with aspect ratios 3.5 and 3.4 for the right- and the left clasts, respectively. The right- and the left clasts of the boudin in **b** have aspect ratios 3.9 and 3.4, respectively. No passive folds are developed along with these boudins due to lack of any foliation planes near them. While in **b**, the extensional force is strong enough to break the single clast but not able to separate them, that in **c** has been stronger to separate the broken pieces. Photos **b** and **c** are in plane- and cross polarized lights, respectively. Both the thin-sections are XZ oriented, from Zanskar Shear Zone. Photo lengths: 0.5 mm. Thin-section numbers: P9/A9 and P9/C, respectively. **d** Lenticular foliation boudin of an aggregate of muscovite grains. The aggregate at the right side is much bigger than that at the left side. The aggregate at the right- and the left hand sides have aspect ratios 3.32 and 4.3, respectively. A *thin white line* demarcates the orientation of the main foliation. Photo in cross polarized light. XZ oriented thin-section from Zanskar Shear Zone. Photo length: 2.5 mm. Thin-section number: P9/G

Existing relevant models

The simple shear model

The simple shear model (Jain and Manickavasagam 1993; Hubbard 1996) explains inverted metamorphism in the Zanskar section of the HHSZ by considering consistent top-to-SW sense of simple shearing (constraint V in "Formulation of the model") along northeasterly dipping numerous planar discrete shear planes (Fig. 17, constraint I in "Formulation of the model") giving rise to extrusion during 22–18 Ma (constraint II in "Formulation of the model"). The metamorphic isograds were kinked on the regional scale in response to simple shearing and gave rise to inverted metamorphism throughout the HHSZ. Along with the P–T data, millimeter- to decimeter scale displacement along the C-planes has been calculated to extrude the HHSZ rocks cumulatively from a depth of at least 30–35 km. Further works (Manickavasagam et al. 1999; Jain et al. 1999, 2002; Tripathi and Gairola 1999) from other sections of the HHSZ provided structural- and thermobarometric data that support this model. The velocity profile for this flow model was originally not given by its proponents, but can be derived as in Eq. 3 in the "Appendix" (line 1 in Fig. 18a). Although a fluid mechanical theory of Couette flow (Schlichting 1955) is implicit in this model, thereby the rocks of the HHSZ are considered to be of fluid character (constraint VII in "Formulation of the model"), the main shortcoming lies in the fact that it cannot explain the presence of a zone of normal sequence of isograds within the upper part of the HHSZ (constraint VI in "Formulation of the model"), the 18–16 Ma old top-to-NE sense of ductile shearing within the ZSZ (constraints III and IV in "Formulation of the model"). Subsequently, conditions of the thickness and the slip rate of the ZSZ (points VIII–X in "Formulation of the model") also remain unexplained.

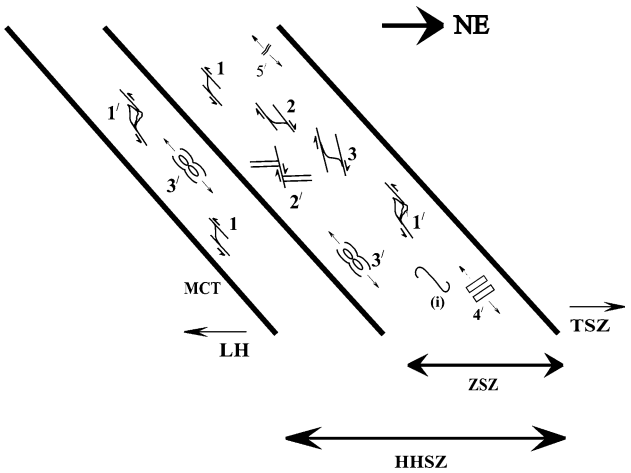

Fig. 16 The dominant structures within the HHSZ, Zanskar section, observed in the NE–SW cross-section, are summarized from the present micro-structural studies, and the previous work—mainly from Jain and Anand (1988). The HHSZ is bounded by northeasterly dipping Main Central Thrust (MCT) and the Lesser Himalaya (LH) at the south; and the top of the Zanskar Shear Zone and the beginning of the Tethyan Sedimentary Zone (TSZ) at the north. Symbols: *half arrows- 1* top-to-SW compressional ductile shearing, *2* top-to-NE extensional ductile shearing; *3* steeper top-to-NE (down) extensional ductile shearing. These shear senses correspond to 'shearing-1', '-2' and '-3' events, respectively. *(i)* hook-shaped fabric; *1′* top-to-SW sense of brittle shearing; *2′* northeasterly steeply dipping brittle normal fault; *3′* boudinaging; *4′* parallel pull apart; *5′* steep fracturing. Different indicators of ductile shear senses have been used to decipher these shear senses, but only the S–C fabrics are shown. *3′* and *4′* imply brittle–ductile- and brittle extension, respectively. Both these extensions are parallel to the main foliation, shown by *arrows*. 'Shearing-2', and possibly also 'shearing-3' and '2′', are exclusively confined within the ZSZ. The diagram is neither to scale nor angle

The channel flow model

During 'channel flow'/'Poiseuille flow', an incompressible Newtonian viscous fluid undergoes laminar flow through infinitely long parallel horizontal static channel walls, due to a pressure gradient (curve 2 in Fig 18a, Eq. 4 in "Appendix") giving rise to parabolic velocity profile. (Pai 1956). Grujic et al. (1996) used the same extrusion mechanism through a divergent-up funnel-shaped Higher Himalayan Crystalline (same as our 'HHSZ') from Bhutan Himalaya (Fig. 17b). In an ideal channel flow through parallel walls, the vertex of this profile is equidistant from the walls. A line passing through the vertex and parallel to the walls divide the channel into two zones of equal thickness with opposite senses of ductile shearing. Since the walls remain static, the fluid extrudes essentially in a simple shearing mode (constraint V in "Formulation of the model"). Intersection between parabolically regionally telescoped isograds with the topography leads to an inverted metamorphism followed by a normal sequence of isograds in the HHSZ (Fig. 18b, constraint VI in "Formulation of the model"). The rate of extrusion increases across the channel from zero at one wall, attains the maximum value at the middle of the channel, and drops symmetrically to zero at the other wall. Ductile shear strain at any instant is zero on the line equidistant from the walls, and increases symmetrically towards both the walls. The channel flow mode of extrusion was considered to initiate at 34 Ma in the sub-horizontal channel at a depth of 25–30 km (Beaumont et al. 2001). Therefore, the extrusion took 16 Ma to arrive the surface at 18 Ma with the first documentation of simultaneous activation of the MCT and the ZSZ. Considering the HHSZ to dip at an angle of 30° (Fig. 2b of Vannay and Grasemann 2001), this means that the partially molten material traveled at least 50–60 km during extrusion. This in turn would indicate the velocity of extrusion of the HHSZ was 3.1–3.8 mm year^{-1}, which satisfactorily comes within the range of 5.0–8.8 mm year^{-1} rate of extrusion of the Zanskar section of the HHSZ as given by Dèzes (1999).

The channel flow model is fluid mechanical and approximately represents the ductile deformation or fluid flow behaviour of the HHSZ (constraint VII in "Formulation of the model"). Considering a southwestward flow of the rocks in the northeasterly dipping planar foliations of the HHSZ (constraint I in "Formulation of the model"), the model produces a zone of top-to-NE sense of shearing characteristic of the STDS/ZSZ but of equal thickness as that of the zone of top-to-SW sense of shearing in the HHSZ. Thus, the model cannot explain the early phase of a top-to-SW sense of ductile shearing in the ZSZ and in its continuation (constraints II and III in "Formulation of the model") nor the thickness constraint of the ZSZ (constraint VIII in "Formulation of the model"). Contrary to constraint VIII in "Formulation of the model", the channel flow model generates a ZSZ of equal thickness as that of the remainder of the HHSZ. Further, the same velocities of flow are produced near the MCT and inside the ZSZ at points that are equidistant from the nearest respective boundaries of the shear zone/channel (curve 2 in Fig. 18a). Thus, a faster rate of extrusion in the ZSZ in comparison to that near the MCT at any specific instant of ductile deformation of the HHSZ (constraint X in "Formulation of the model") remains unexplained. For an increase or a decrease in the pressure gradient, the vertex of the parabolic profile attains a higher or a lower velocity, respectively. On other hand, with any increase or decrease in viscosity, the parabolic profile is merely less or more tapered, respectively. In these two possible cases, the vertex remains equidistant from the channel walls. For a specific thickness of the HHSZ, therefore, variation in the thickness of the ZSZ over local- and regional scales (constraint IX in "Formulation of the model") cannot be explained by variation in the flow parameters viz. the

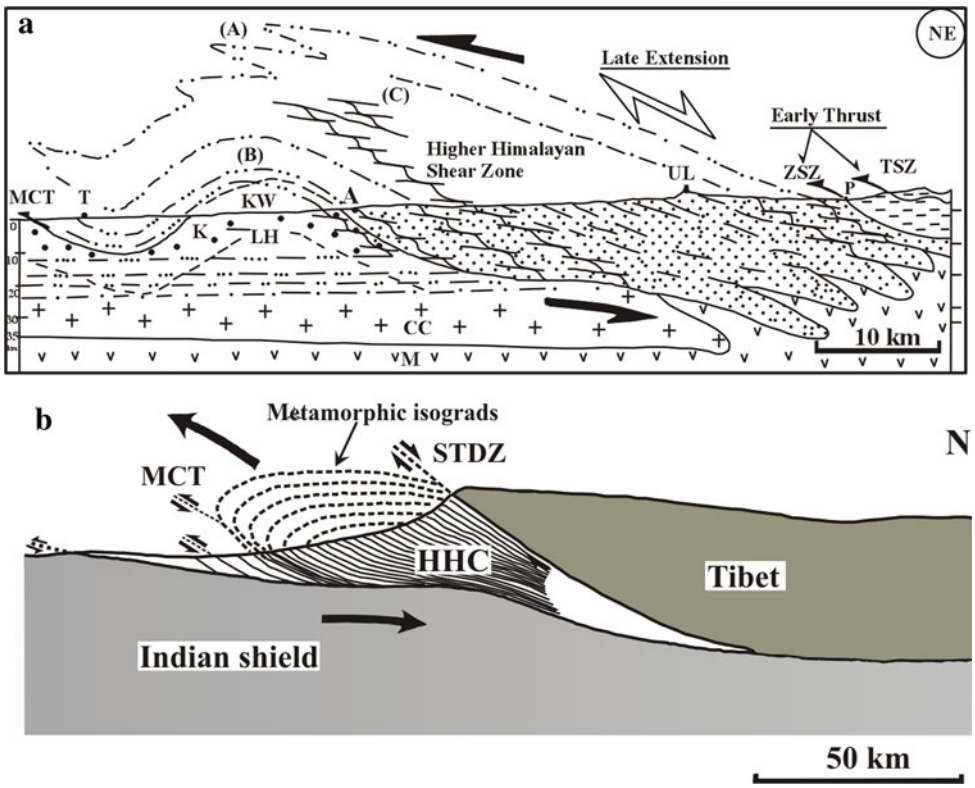

Fig. 17 **a** Distributed simple shear model of extrusion of the HHSZ showing northeasterly/northerly dipping S-planes and the isograds. Possible superposed effects of post-metamorphic overturned and/or recumbent folding (*A*), and thrusting like the MCT (*B*), and zones of ductile high strains (*C*) on isograds, causing inverted metamorphism are shown. *Double thick arrows*, *single arrows*, and *double open arrow* represent early ductile compressional shearing, discrete thrusts and late extensional ductile shearing, respectively. Symbols- *LH* Late Proterozoic sedimentary sequence of the Kishtwar Window (KW), *TSZ* Tethyan Sedimentary Zone; *CC* continental crust of the Indian plate; *M* upper mantle, *T* Thatri, *K* Kishtwar, *A* Atholi, *UL* Umasi La, *P* Padam. Metamorphic isograd boundaries are represented by *dash-dot lines*. Reproduced from Jain and Manickavasagam (1993) and Jain et al. (2002). **b** Channel flow model of extrusion of the HHSZ through its wedge-shaped geometry in Bhutan Himalaya. The term 'Higher Himalayan Crystallines (HHC)' has been used to represent the HHSZ. The extrusion of partially molten HHSZ crust gives rise to megascopic telescoping of the metamorphic isograds. Symbols- *MCT* Main Central Thrust, *STDZ* South Tibetan Detachment Zone (a continuation of the Zanskar Shear Zone). Subduction of the Indian shield below the Tibetan plate is shown by a *thick arrow*. Reproduced from Grujic et al. (1996)

viscosity of fluid and the pressure gradient guiding the flow.

The proposed model

To satisfy all the constrains listed in "Formulation of the model", the following analytical model based on the solution of a simplified form of the Navier Stokes equation at geologically realistic physical boundary conditions is proposed as the mechanism of extrusion within the ductile regime of the HHSZ in the Zanskar section. The presented model is elaborations of Figures 6a, b in Grujic et al. (2002) in terms of statements of physical boundary conditions that drove these flows and the algebraic forms of their velocity profiles presented in this work. The model involves a combination of simple shear of the boundaries of the HHSZ and a channel flow, and is henceforth referred as the 'combined flow' model. The top boundary of the HHSZ (same as that of the ZSZ) and the MCT are considered to be static and parallel walls of a very long channel full of a Newtonian viscous fluid (constraint VII in "Formulation of the model"). The model assumes flow lines and imaginary inactive markers at angles to them to be comparable with the primary shear planes and shear fabrics, respectively. Since no turbulence is permitted in the combined flow model, the flow lines essentially remain parallel during the extrusion process. Considering the channel to be northeasterly dipping and a southwestward extrusion of fluid through it (Fig. 18a) constraint-I in "Formulation of the model" about the parallelism and dip direction of the shear planes of the HHSZ are obeyed. The consideration of rheology of real rocks as Newtonian is certainly an approximation (Ramsay and Lisle 2000), but has previously been adopted in similar tectonic modeling to explain the first order tectonic constraints of mountains (e.g., Beaumont et al. 2001). The fluid inside the channel, an analogue to the

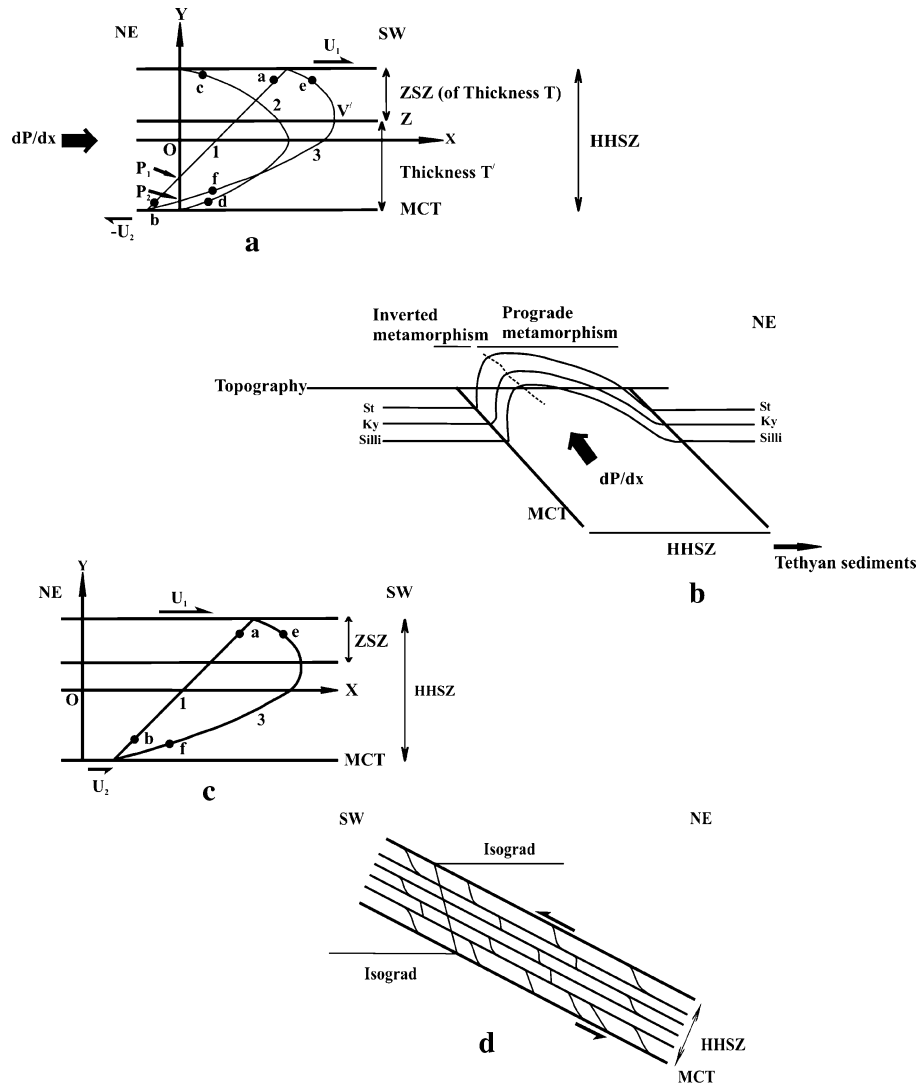

Fig. 18 **a** We consider a channel with horizontal, infinitely long and NE–SW oriented static walls, full of an incompressible Newtonian viscous fluid. Orthogonal coordinate axes are chosen with the *X*-axis parallel to, and equidistant from the walls. An inactive marker, coincident with the *Y*-axis is considered at the onset of flow. *Line 1* velocity profile of simple shear deformation in the E_1-phase when the top and the bottom walls are sheared with velocities U_1 and U_2, respectively, maintaining $dP/dx = 0$. Pivot point P_1: over this point the marker in the E_1-phase rotates in progressive strain. Parabola-2: channel flow where $U_1 = U_2 = 0$, and $(dP/dx) \neq 0$. *Solid arrow*: direction of fluid flow in response to the pressure gradient. Parabola-3: the E_2-phase, combined simple shear and channel flow i.e., $(dP/dx) \neq 0$, and U_1 and/or $U_2 \neq 0$. V' vertex of parabola-3, located within the upper part of the channel. Z a line passes through V', parallel to the walls, demarcates the lower boundary of the ZSZ. T and T': thicknesses of the ZSZ and that of the remainder of the HHSZ, respectively. Pivot point P_2 intersection between profile-3 and the *Y*-axis, the marker remains attached at this point while becoming progressively tapering parabolas with increasing strain. For flow profile-1, any point *a* near the top of the channel extrudes faster than the location *b* near the bottom. For flow profile-2, the points equidistant from the walls, *c* and *d*, extrude with same rate. For flow profile-3, any point *e* within the model ZSZ has got higher rate of extrusion in the southwest direction than that any point *f* near the MCT. The diagram is not to scale. **b** Effect of channel flow- (profile '2' in **a**) and combined flow (profile '3' in **a**) mode of extrusion through northeasterly dipping HHSZ in telescoping staurolite (st), kyanite (ky) and sillimanite (silli) isograds. Intersection between these regionally warped isograds with the topography leads to a zone of inverted metamorphism in the southwest followed by a normal sequence of metamorphic zones in the northeast. These two zones are separated by a *dotted line* in the diagram. **c** We consider a channel with the geometry, geographic orientation and rheology same as that of **a**. A second possible flow situation of the E_1- and the E_2-phases of extrusion are demonstrated with the velocity profiles '1' and '3' for which $U_1 > U_2 > 0$ and $dP/dx = 0$; and $U_1 = U_2 = 0$ and $dP/dx \neq 0$; respectively. The structural and metamorphic significances of these phases remain the same as that of **a**. Any points *a* and *e* near the top of the channel extrudes faster than that near the bottom at any locations *b* and *f* for the two respective phases. No pivot exists in these flow cases. **d** Structural and metamorphic significance of the E_1-phase of extrusion is represented by S–C fabrics and inactive metamorphic isograds, respectively. The HHSZ demonstrates consistent top-to-SW sense of ductile shearing. The isograds are regionally kinked into top-to-SW sense giving rise to inverted metamorphism in the HHSZ. This is demonstrated with a single isograd. The diagram is neither to scale nor angle

rocks of the HHSZ and is also considered to be incompressible. Therefore, the kinematic effects of dilatancy due to partial melting (Grasemann et al. 2006) are neglected.

The combined flow model of extrusion of the HHSZ during 22–16 Ma is divided into two phases: $E = E_1 + E_2$. These phases are exemplified with the help of minimum but most crucial flow parameters that explains the extrusion. These are (1) a pressure gradient component, (2) the thickness-, (3) the viscosity of the rocks-, and (4) the relative rate of slip of the boundaries of the HHSZ. While the E_1-phase utilizes the second- and the fourth parameter only, the E_2-phase is based on all of them. The choice of minimum number of parameters here is in contrast to the classical channel flow model proposed and nurtured by the Dalhousie research group (Beaumont et al. 2001, 2004; Jamieson et al. 2004) that involves input of additional parameters such as density-, thermal conductivity, and the rate of erosion of the extruded rock. However, those parameters do not have direct relations with the first order constraints of extrusion (Grasemann et al. 2006). Both during the E_1- and the E_2-phases, no component of movement of the walls of the channel exist towards each other. Rocks extrude essentially by slow laminar flow parallel to the channel walls. Thus, these phases assume flow by simple shear (constraint V in "Formulation of the model").

The E_1-phase (line 1 in Fig. 18a, c)

The top-to-SW sense of ductile simple shearing of the boundaries of the HHSZ is represented by a linear velocity profile (Eq. 3 in the "Appendix"). The sense of shearing and the ductile shear strain at any instant inside the channel remain the same. The velocity of different layers within the channel falls linearly from the top- to the bottom boundary. We consider two possible flow cases of the E_1-phase as follows. The top-to-SW sense of shearing in the HHSZ can be generated either by (1) absolute movements of the top of the ZSZ/HHSZ and the MCT towards SW and NE, respectively, or (2) both of them move southwestward but the former with a higher velocity. In the first case, a pivotal point exists across which any imaginary marker initially non-parallel to the MCT keeps rotating on progressive simple shearing (line 1 in Fig. 18a). The position of this pivot depends on the absolute velocity of the walls and the thickness of the channel (see the expression after Eq. 4 in the "Appendix"). However, the pivot does not exist in the second case (line 1 in Fig. 18c). During the E_1-phase of extrusion, the ZSZ characterized by a top-to-NE sense of shearing was not produced within the top of the HHSZ. The E_1-phase takes into account the extrusion of the HHSZ during 22–18 Ma, the Himalayan D_2 deformation phase of Vannay and Grasemann (2001) and Jain et al. (2002) and development of shear sense indicators with a consistent top-to-SW sense of shearing throughout the shear zone (Fig. 18d, constraint II in "Formulation of the model"). In other word, the E_1-phase is the mathematical representation of simple shear model of Jain and Manickavasagam (1993) and Hubbard (1996).

The E_2-phase (curve 3 in Fig. 18a, c)

During this phase of extrusion, viscosities of the rocks constituting the HHSZ were significantly reduced and extruded southwestward like a fluid by a combination of the pressure gradient inducing a channel flow in addition to the ongoing top-to-SW sense of shearing of the MCT and the top of the ZSZ. Protracted partial melting, anatexis, migmatization, and leucogranite injection within the structurally higher parts of the HHSZ including the ZSZ during this period (Dèzes et al. 1999; Jain and Patel 1999) denote the fluid character of the rocks. The E_2-phase takes into account the extrusion of the HHSZ during 18–16 Ma period of simultaneous compressional shearing of the MCT and the extensional shearing of the ZSZ (constraint III, IV in "Formulation of the model"). The rocks at the base of the over-thickened Tibetan plateau were partially molten possibly due to elevated pressure and temperature and acted as a source of molten rock materials within the upper part of the HHSZ. The flow in the HHSZ is represented by a parabolic velocity profile (Eq. 5 in the "Appendix"), which is a vector addition of the velocity profiles of the E_1-phase and that of the channel flow component (see the expression immediately after Eq. 7 in the "Appendix"). The vertex of the velocity profile is located within the upper half of the channel (the expression after Eq. 6 in the "Appendix"). Across the line passing through the vertex and parallel to the MCT, the sense of ductile shearing is opposite. This line is the lower boundary of the ZSZ, below and above which lie zones that undergo a top-to-SW compressional and a top-to-NE extensional shearing, respectively, and is not a lithological discontinuity. The compressional shearing can be viewed as a part of the D_2 deformation phase of Vannay and Grasemann (2001) and Jain et al. (2002). Equations 6 and 7 in the "Appendix" show that, under the combined activation of simple shear and channel flow, the model ZSZ is thinner than that of the remainder of the HHSZ (constraint VIII in "Formulation of the model").

During the E_2-phase, had the pressure gradient component acted along with the first flow possibility of the E_1 phase, i.e., movement of the top and the bottom walls of the HHSZ in opposite directions, a pivotal point should exist. Across this pivot, any imaginary inactive marker initially non-parallel to the walls of the shear zone keeps deforming into progressively tapering parabolas (curve 3 in Fig. 18a). The position of this pivot depends on all the four flow

parameters that define the velocity profile (see the algebraic expression after Eq. 4 in the "Appendix"). However, the pivot would not exist if the pressure gradient component characteristic of the E_2-phase had acted along with the second flow case of the E_1-phase, i.e., movement of both the boundary walls of the HHSZ towards southwest direction (curve 3 in Fig. 18c). Given the uncertainty in the direction of absolute movement of the boundaries of the HHSZ, a search for the location of the pivot in field for the E_1- and the E_2-phases would not be a useful exercise.

During the E_2-phase, both the top- and the bottom boundaries of the ZSZ underwent southwestward shearing with the later boundary moving at a higher velocity. This gave rise to a southwestward extrusion vis-à-vis a perceptible top-to-NE sense of shearing in the ZSZ (Fig. 19a, b; constraint III in "Formulation of the model"). While many shear fabrics were produced showing a top-to-NE sense of ductile shearing (Fig. 2a, 3a, c, 4b–d, 5b, 6a–d) in the ZSZ, most of the early fabrics indicative of a top-to-SW sense were destroyed but very few escaped this retro-shear along the same C-planes possibly due to strain partitioning and survived as remnants (Figs. 2a, b, 3a). Rarely, S-fabrics of the E_1-phase that enjoyed strong shear sense reversal modified their shapes into hooks (Fig. 8a, c).

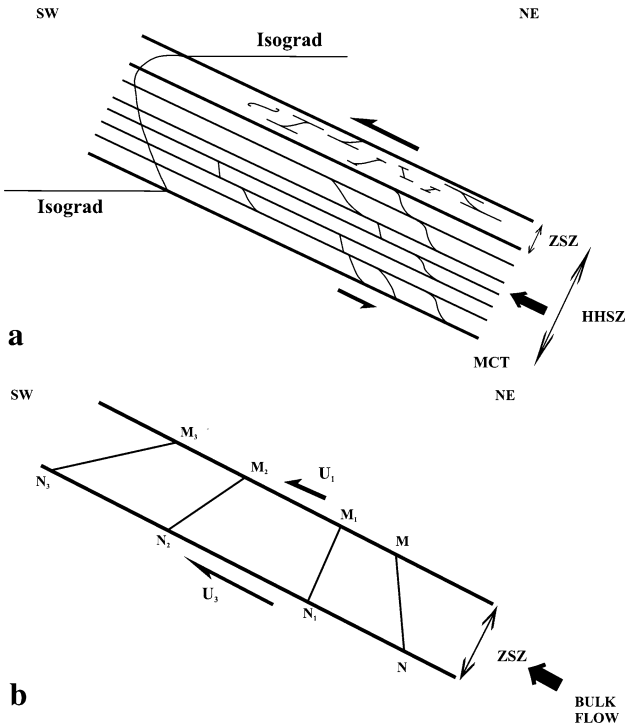

Fig. 19 **a** Structural and metamorphic significance of the E_2-phase of extrusion are shown on a channel possessing the geometry, geographic orientation, and rheology same as that of Fig. 18a. U_1 and $-U_2$ are the shear velocities of the upper- and the lower wall, respectively. The *solid arrow* represents the direction of flow of the fluid under a pressure gradient. The isograds are deformed into parabolas similar to the velocity profile giving rise to inverted metamorphism within the HHSZ. This is demonstrated with a single isograd. Within the ZSZ, a top-to-NE sense of ductile shearing is produced even within the regime of bulk southwestward flow. The remainder of the HHSZ undergoes consistent top-to-SW sense of ductile shearing. Not to scale. **b** Reorientation of the ductile shear fabric MN within the ZSZ during the E_2 phase. As a result of the E_1-phase, MN achieved a top-to-SW sense of orientation. When the E_2-phase began, the lower- and the upper boundaries of the ZSZ moved with velocities U_3 and U_1 ($U_3 > U_1$), respectively. The expression of U_3 is given between Eqs 5 and 6 in the "Appendix". Bulk southwestward flow reoriented this fabric into M_1N_1, into M_2N_2, and finally into M_3N_3. This gives rise to a top-to-NE sense of shearing at the final M_3N_3 orientation. Not to scale

Discussion

According to the proposed extrusion model, the thickness of the ZSZ is dependent on all the four flow parameters that define the velocity profile of the E_2-phase (Eq. 5 in the "Appendix"). The E_2-phase of extrusion of the HHSZ continued over 2 Ma unlike what has been postulated for a purely channel flow mode of extrusion for a greater span approximately from 12 to 24 Ma (Harris 2007 and references therein). The geographic extent of activation of the combined flow is also expected to be quite large within the HHSZ along the entire trend of the Himalaya. Over such a wide spatial- and temporal extent, the flow parameters vary as follows. (1) *Pressure gradient*: the pressure gradient giving rise to the Poiseuille flow mode of extrusion used to be 3.5 kbar km^{-1} (Searle 1999), 0.28 ± 0.17 kbar km^{-1} (Searle et al. 1992) or 0.2885 kbar km^{-1} (Walker et al. 2001) in the Zanskar Himalaya. It had a similar magnitude of 0.27 kbar km^{-1} in the Nepalese Himalaya (Hodges et al. 1988), 0.33 kbar km^{-1} at the late stage of the combined flow during a relatively shorter time span between 16 and 13 Ma (Hollister and Grujic 2006), or 0.3 ± 0.08 kbar km^{-1} in the Langtang valley, Nepal (Fraser et al. 2000), and about ten times higher value ranging from 1 to 2 kbar km^{-1} (Grujic et al. 2002), or a still higher magnitude of 3.71 kbar km^{-1} in the footwall of the ZSZ (Walker et al. 1999), 5–6 kbar km^{-1} at the base of the HHSZ in the Nepal Himalaya (Kohn 2008), and 6 kbar km^{-1} at the MCT in Central Nepal (Catlos 2000). (2) *Viscosity*: the viscosity of the partially molten rock at a mid-crustal depth, now extruded at the surface, was $\sim 10^{19}$ Pa s (Jamieson et al. 2004); but that of the molten granite extruded in a prodigious proportion in the upper part of the HHSZ could have been as low as 10^5–10^{12} Pa s (Druguet and Carreras 2006 and references therein) or $10^{4.5}$ Pa s (Scaliot et al. 1996). The viscosity of the molten rock is expected to temporally increase due to progressive reduction in its temperature as it keeps extruding at shallower crustal levels. (3) *The rate of slip of the boundaries of the HHSZ*: the rate of slip of the MCT in different sections ranged from few mm per year, e.g., 1.2 mm year^{-1} (Valdiya

2001), 3–5 mm year^{-1} (Yin 2006), up to an exceedingly slow rate of 0.8 mm year^{-1} in the Nepal Himalaya (Wobus et al. 2005). (4) *The thickness of the HHSZ*: in different sections, the thickness varies from 10 km as the lowest reported value (Grasemann and Vanney 1999) to a maximum of 50 km (Jain and Anand 1988).

In order to generate a top-to-SW sense of shearing, both the possible flow cases of the E_1-phase intrinsically assume that the top part of the HHSZ was extruded at a faster rate than the bottom part. The constraint of faster extruding upper part of the channel is also maintained during the E_2-phase when the pressure gradient component acts along with either of the flow possibilities of the former E_1-phase (constraint X in "Formulation of the model"; lines 1, 3 in Fig. 18a, c).

As revealed in the present micro-structural studies of the ZSZ, the porphyroblastic index minerals of high-grade metamorphism such as staurolite and sillimanite were affected by the top-to-SW followed by ductile extensional shearing on the micro-scale (Figs. 2a, b, 4a, 8a, c). Jain et al. (2002) made a similar micro-structural observation on staurolite, kyanite, and sillimanite porphyroblasts from the high-grade rocks in the ZSZ. These observations are interpreted in this study as follows: (1) the higher grade metamorphism in the ZSZ did not predate the end of the top-to-NE sense of shearing event between 18 and 16 Ma, i.e., it is no younger than $\sim$16 Ma; and (2) the isograds in the ZSZ, therefore, also in the whole of the HHSZ defined by these index minerals, were deformed by the ductile shearing events. The effectiveness of (a) simple shearing of isograds in millimeter-scale along C-planes in giving rise to their displacement for tens of kilometers or so on the regional scale, and (b) subsequent inverted metamorphism has previously been explained texturally from the HHSZ in the Zanskar section by Jain and Manickavasagam (1993) and analytically by Grasemann and Vanney (1999). A similar extrusion mechanism considering the isograds to be inactive markers has also been visualized in terms of regionally telescoped isograds from the Zanskar section by Stephenson et al. (2001) and Searle et al. (1992), and from Bhutan Himalaya by Grujic et al. (1996). In the combined model, we propose that isograds were deformed similar to the velocity profiles of the respective phases of extrusion, i.e., they were first sheared into a top-to-SW sense giving rise to inverted metamorphism from the MCT up to the top of the HHSZ during 22–18 Ma of the E_1-phase (Fig 18d). These isograds were modified into parabolas during the subsequent E_2-phase (Fig. 19a). In response to the south-westward gravitational spreading of the extruded HHSZ, due to existing topographic highs in the northeast, the vertices of the parabolic isograds shifted more towards the MCT. Each of the isograds intercepted the topographic surface at two lines (Fig. 18b) similar to what was postulated for a purely channel flow extrusion mode. On a northeastward traverse from the MCT, this gave rise to an inverted- followed by a normal sequence of metamorphism (constraint VI in "Formulation of the model"). While the presented combined flow model satisfies all the constraints in "Formulation of the model" as discussed above, it makes the following conjectures.

Speculation 1

The ductile shear strain at any point inside the HHSZ at any instant during, and also at the end, of the E_1-phase should be the same. This is because at any moment the angle between the marker and the shear planes (flow lines) remain the same throughout the channel. However, this is not possible to check in the field since the extrusion phase was later superposed by the E_2-phase of extrusion and deformation with spatial variation in the ductile shear strain parameter.

Speculation 2

The ductile shear strain in the E_2-phase at any point on the profile is defined by the 'tan' of the acute angle between the tangent at that point and the *Y*-axis. During and after the end of the E_2-phase, the instantaneous ductile shear strain is speculated to progressively fall to zero from either boundaries of the HHSZ towards the lower boundary of the ZSZ. A large amount of simple shearing deciphered from the kinematic vorticity numbers at the boundaries of the HHSZ, 0.66–0.77 near the MCT in the lower Dolpo range in the western Nepal, 0.67–0.98 in the STDS in the Mt. Everest region; and its lesser range of magnitudes inside the shear zone e.g., 0.66–0.76 in the western Bhutan (Carosi et al. 2007 and references therein) crudely supports this prediction. We note that, after the ductile extrusion ceased, the angle between the S- and the C fabrics in the HHSZ would not necessarily show any systematic variation in a NE–SW transect. This is because the final angle between the two fabric depends on (1) the angle between these two foliations before ductile shearing took place; (2) whether the S-fabric is strain sensitive or -insensitive (Davis and Reynolds 1996); and (3) probable strain partitioning within the shear zone. Therefore, these angles are not measures of ductile shear strain, nor should their spatial variation be used to validate the proposed model.

Speculation 3

The parabolic velocity profile characteristic of the E_2-phase is also a representation of a spatial variation of extrusion rates in the HHSZ. Thus, the E_2-phase envisages that the base of the ZSZ extruded at the fastest rate (see the

expression between Eqs. 5 and 6 in the "Appendix"), and that the extrusion rate falls off from the base of the ZSZ towards its walls. To check its validity, the rate of extrusion at a number of locations across the HHSZ when the E_2-phase was active between 18 and 16 Ma is needed, but is lacking in the Zanskar section. A similar data set with an average value of 1.4 ± 0.2 mm year^{-1} for the entire shear zone, determined from apatite fission track young ages, is available from the Sutlej section of the HHSZ (Thiede et al. 2004). However, the data cannot be used since (1) it is valid between Pliocene–Quaternary time i.e., ~11 Ma after the possible end of the E_2-phase, and (2) a high rate of erosion of the shear zone has a strong control on this data (Thiede et al. 2004).

Speculation 4

For certain combinations of the four flow parameters controlling the E_2-phase-pressure gradient, relative slip rate of the walls, viscosity and thickness of the HHSZ, it is shown that the vertex of the parabolic profile touches the upper boundary of the HHSZ (curve 4 in Fig. 20, Eq. 8 in the "Appendix"), or may go even outside the shear zone (curve 5 in Fig. 20, Eq. 10 in the "Appendix"). Quite interestingly, in the former flow case, the velocity profile is independent of viscosity (Eq 9 in the "Appendix"). In both the flow situations, the HHSZ should demonstrate a uniform top-to-SW sense of ductile shearing and no ZSZ is produced even if a component of channel flow is active. The situation is therefore structurally equivalent to the previous E_1-phase. Thus, a continuation of the ZSZ/STDS, might be lacking in some sections of the HHSZ even if a pressure gradient drives the extrusion along with the simple shearing of the walls. Thus, if a continuation of an extensional ductile shear zone is not present within the top of the HHSZ at some section, it does not necessarily mean that the channel flow component was absent there during 18–16 Ma span. To check whether such an extrusion mechanism was active in a section of HHSZ displaying uniform top-to-SW sense of shearing and an absence of a ductile extensional shear zone, the following points are to be satisfied within 18–16 Ma range: (a) the ductile shear strain within the HHSZ has to keep falling from the MCT towards the upper boundary of the shear zone; (b) the rate of extrusion should keep increasing from the MCT towards the upper wall; and (c) from the base to the top, the HHSZ should demonstrate inverted metamorphism and no zone of normal sequence of metamorphism should be present. A part of the Kashmir Himalaya in India from Zanskar till the Nanga Parbat metamorphics is characterized by an absence of the ZSZ/STDS. The available explanation is that the ZSZ/STDS has been a blind structure there (Yin 2006 and references therein) although, this idea is not substantiated by any further evidences. If this part of the HHSZ can satisfy the three above mentioned points, an alternate explanation of special combinations of the flow parameters leading to the absence of the ZSZ/STDS could be posed.

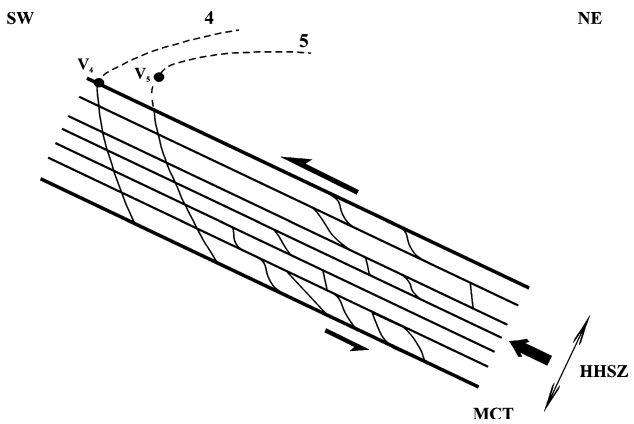

Fig. 20 Two special cases of the E_2 phase of extrusion are represented by the parabolic velocity profiles 4 and -5 in a northeasterly dipping NE–SW cross-section of the HHSZ. Within the flow domain of the HHSZ, the profiles are represented by *solid lines*. The profiles are extrapolated by *dashed lines* outside the flow domain in order to show that they are parabolas and the location of their vertices V_4 and V_5, respectively. The top-to-SW sense of simple shearing of the walls is shown by *half arrows*. The direction of flow of fluid in response to the pressure gradient is shown by a *solid arrow*. V_4 and V_5 lie on the upper boundary and outside the HHSZ, respectively. In both these situations, a consistent top-to-SW sense of ductile shearing persists throughout the HHSZ and is manifested by S–C fabric and other shear sense indicators. The diagram is neither to scale nor angle

Speculation 5

It is important to note that single- (Figs. 2a, b, 3a–d, 4a–d, 5b, 6a–d, 7a–d) and double shear senses (Figs. 8a, c) of ductile deformation given by different micro-fabrics in the ZSZ is taken as one of the constraints in "Formulation of the model" to establish the present tectonic model. For any initial orientation other than that parallel to the boundaries of the shear zone, planar foliation planes, and straight grain boundaries, under the E_1 and the subsequent E_2 extrusion phases are supposed to be planar and parabolic, respectively, in conformity to their velocity profiles. Since the ductile shear strain during and at the end of the E_2-phase should ideally be most intense near the boundaries of the channel, parabolic fabrics are expected to strongly develop near the MCT and within the ZSZ. Contrary to this prediction, but as in any shear zone (Passchier and Trouw 2005) and also in the remainder of the HHSZ (e.g. Jain et al. 2002 and references therein), the observed shear fabrics and grain boundaries in the ZSZ are sigmoidal (Figs. 2a, 4c, 7a; grain 'n' in Fig. 7c), elliptical (grain 'm' in Fig. 7c), and straight (Fig. 7b), but not parabolic. The behaviour of single or aggregates of

mineral(s) as heterogeneous strain markers (Treagus et al. 1996) seems to be the key reason for deviation from the simplest prediction. For example, even if simple shear with an overall linear velocity profile is imposed on a composite of matrix and square-shaped clasts, the clast may acquire curved boundaries depending on the viscosity contrast between them and the matrix (Treagus and Lan 2004 and references therein). Though not studied in this work, the shape of the clasts under combined flow regime may, therefore, be different from the parabolic profile.

Different phases of brittle deformation events, assuming they are younger than the lower age limit of the E_2-phase $\sim$16 Ma, signals the cessation of the ductile E_2-phase as the hot partially molten HHSZ rocks crossed the brittle–ductile regime, possibly at 8 km depth (Davis and Reynolds 1996), and entered the brittle deformation regime. The pressure gradient responsible for the fluid flow behaviour of the HHSZ of the E_2-phase stopped near this interface. However, the top-to-SW sense of shear component (U_1 and U_2 in Fig. 18a, c) that was active at 22 Ma, continued in terms of brittle shearing along the pre-existing ductile primary shear planes. This is revealed by asymmetric duplexes (Fig. 9a–c) and V pull-aparts (Fig. 12a–c) with their Y-planes coincident with the C-planes at the grain-scale in the ZSZ. This brittle shearing event might have facilitated the ductilely extruded rocks of the HHSZ to arrive at a still shallower crustal depth. Finally, late-stage brittle normal faulting (Fig. 13a, b) and fracturing (Fig. 14a, b) that cut the primary shear planes at high angles indicated texturally the termination of the top-to-SW shearing event of the brittle regime. A phase of brittle–ductile deformation gave rise to extension of the mineral grains to variable degrees (Fig. 15a–d) along the primary shear planes, but probably did not help the extrusion.

Conclusions

The Zanskar Shear Zone (ZSZ) in the Suru Doda valley of NW Indian Himalaya demarcates the northern boundary of the Higher Himalayan Shear Zone (HHSZ), and is characterized by a top-to-NE sense of ductile shearing. The deformation phases of the rocks of the ZSZ, identified under a microscope, are (1) 'shearing-1': initial top-to-SW sense of ductile shearing, survived as remnants, along northeast dipping C-planes (the main foliation); (2) 'shearing-2': subsequent strong top-to-NE sense of ductile shearing along the same main foliations; (3) 'shearing-3': very strong ductile shearing, synthetic to the previous shearing phase, along steeply northeast dipping planes at an angle to, and cutting the previous shear fabrics; (4) differential local brittle–ductile extension parallel to the main foliation, indicated by boudins of different varieties with low and limited range of aspect ratios; (5) a top-to-SW sense of brittle shearing along the main foliation, determined from asymmetric duplexes of a number of minerals—mostly micas, and V-pull aparts of originally single mineral; (6) northeasterly steeply dipping synthetic Riedel shear (brittle faults) that displaces individual mineral grains; (7) brittle extension parallel to the main foliations, given by parallel pull aparts; and (8) northeasterly steeply dipping T-fractures. Different phases of ductile deformation are deciphered using S–C fabrics, mineral fish of various morphological types, intrafolial folds and preferred orientation of grains. The primary shear planes for 'shearing-1' event preferentially acted as the planes for the subsequent 'shearing-2' event and also for the later top-to-SW sense of brittle shearing. The sequence of 'shearing-1' and '-2' is recorded in rare hook-shaped minerals. Hook-shaped minerals are new findings from this study from the ZSZ. Duplexes in grain-scales are also new observations. The thrust-up mineral grains, at micro-scales, acquire the characteristic shape of trapezium or a hat. Hat-shaped grains that are (1) isolated from the underthrust grain, and (2) possibly produced due to migration of boundaries of the adjacent grains are exempted from brittle shear sense determination.

The deformation phases deciphered from the ZSZ, and those previously reported from the remainder of the HHSZ are summarized in a schematic NE–SW cross-section of the shear zone. Matching the observed structures at micro-scale with those previously reported from field-scale, 'shearing-1' is inferred to have been active during 22–18 Ma and continued during 18–16 Ma when 'shearing-2' was also active. A two-phase extrusion model $E = (E_1 + E_2)$ of the Zanskar section within the HHSZ in the ductile regime is presented in this work based on minimum and most critical extrusion parameters. Velocity profiles of these phases are derived assuming the rocks in the HHSZ to have an incompressible Newtonian viscous rheology. In the simple shear model, the E_1-phase is represented by a top-to-SW sense of simple shearing of the parallel walls of the HHSZ during 22–18 Ma. The E_1-phase takes into account the top-to-SW sense of shearing throughout the HHSZ. In the E_2-phase during 18–16 Ma, the HHSZ extruded like a fluid driven by a pressure gradient in addition to the ongoing component of top-to-SW sense of simple shearing of the previous phase of extrusion. This combined flow gave rise to a ZSZ thinner than the remainder of the HHSZ and characterized by an apparent top-to-NE sense of shearing in the upper part of the HHSZ during a bulk southwestward flow. Metamorphic isograds within the HHSZ were deformed into the same geometries as the velocity profiles of the respective phases. The combined flow model enumerates that during the E_1-phase, the whole of the HHSZ underwent inverted metamorphism. In the subsequent E_2-phase, from the MCT towards northeast, this was succeeded

by an inverted- followed by a normal sequence of metamorphism. The spatially variable thickness of the ZSZ at local scale as well as along the Himalayan trend is explained by a wide deviation from section to section in values of (1) relative rate of slip of the boundaries, (2) viscosity of the rocks, (3) pressure gradient, and (4) total thickness of the HHSZ. The combined flow model predicts the followings. (1) Ductile shear strain in the HHSZ at any moment during and also at the end of the E_1-phase was uniform. Since the HHSZ underwent the next extrusion phase, this conjecture is not possible to crosscheck. (2) After the E_2-phase, ductile shear strain was most intense at the boundaries of the HHSZ and progressively reduced towards the base of the ZSZ. Compiled shear strain data from different sections of the HHSZ tentatively supports this idea. (3) The base of the ZSZ underwent the highest rate of extrusion. (4) The ZSZ characterized by a top-to-NE sense of ductile shearing might be absent in some sections of the HHSZ even though a component of the pressure gradient in the E_2 extrusion process was present. These two surmises are not possible to crosscheck immediately due to a paucity of suitable data. (5) Had they behaved as inactive markers, the ductile shear fabrics after the E_2-phase should become parabolic. Micro-textural observations in this work do not fit with the last prediction indicating heterogeneous deformation of minerals in real rocks. The top-to-SW sense shearing, one of the components driving extrusion in the E_2-phase persisted as a pre-16 Ma event in terms of duplexes and V-pull aparts even in the early phase of brittle deformation regime. Successive new generations of brittle deformations such as fracturing and secondary shearing registered the end of this shear component when the extruded rocks arrived at a much shallower crustal depth.

Acknowledgments SM acknowledges Council for Scientific & Industrial Research's Senior Research Fellowship (9/143(441)2001-EMR-I), Swedish Institute's 'Guest Scholarship' during 2005–2006, and the 'seed grant' of IIT Bombay. HAK was supported by the 'Swedish Research Council'. Constructive review by B.C. Burchfiel is appreciated. C.J. Talbot improved the English.

Appendix

Simple shear flow (line 1 in Fig. 18a)

Steady plane laminar flow of an incompressible Newtonian fluid within an infinitely long channel with parallel- and horizontal walls is given by

$$dP/dx = \mu(d^2x/dy^2) \tag{1}$$

(vide p.60 in Schlichting 1955) where dP/dx: pressure gradient along X-direction, μ: viscosity. Putting $dP/dx = 0$. for simple shear,

$$(d^2x/dy^2) = 0. \tag{2}$$

Integrating twice, taking the channel thickness '$2y_o$'; and velocity of walls $x = -U_2, U_1$ at $y = -y_0, y_0$, the flow profile is:

$$x = 0.5(U_1 - U_2) + 0.5y\,y_0^{-1}(U_1 + U_2). \tag{3}$$

Putting $x = 0$ in Eq. 3, the coordinate of the pivot defined by intersection between the Y-axis and the velocity profile is $P_1 \equiv [0, y_o\,(U_1 - U_2)\,(U_1 + U_2)^{-1}]$

Channel flow/Poiseuille flow (curve 2 in Fig. 18a)

Here U_1, $U_2 = 0$ at $y = +y_0$, $-y_0$, dP/dx is a non-zero constant. Integrating Eq. 1 twice and using these boundary conditions, the profile is given by, as Pai (1956),

$$x = -0.5\mu^{-1}(dP/dx)\left(y_0^2 - y^2\right). \tag{4}$$

The co-ordinate of the vertex of this parabolic profile is given by $[0.5\ \mu^{-1}\ y_0^2\ (dP/dx), 0]$.

A combination of simple shear and channel flow (curve 3 in Fig. 18a)

Here U_1 and/or U_2, $dP/dx \neq 0$. Integrating Eq. 1 twice and using the boundary conditions: $x = -U_2$, $+U_1$ for $y = -y_0$, $+y_0$, the velocity profile is given by:

$$x = 0.5(U_1 - U_2) + 0.5y_0^{-1}y(U_1 + U_2) - 0.5\mu^{-1}(dP/dx)(y_0^2 - y^2) \tag{5}$$

From Eqs 3, 4, and 5, x(combined flow) = x(simple shear) + x(channel flow)

The parabolic profile given by Eq. 5 has its vertex at:

$$\begin{aligned} &x-\text{ordinate}: 0.5(U_1-U_2)-0.125y_0^{-2}(U_1+U_2)^2\mu(dx/dP) \\ &\quad -0.5\mu^{-1}y_0^2(dP/dx) \\ &y-\text{ordinate}: -0.5y_0^{-1}\mu(U_1+U_2)(dx/dP). \end{aligned} \tag{6}$$

The maximum value of the x-ordinate on profile Eq. 5 is obtained at the vertex. Therefore, the fluid attains highest velocity $U_3 = x$-ordinate at the vertex. The thickness of the ZSZ and the remainder of the HHSZ, respectively are:

$$\begin{aligned} T &= \left[y_0 - 0.5y_0^{-1}(U_1 + U_2)\mu(dP/dx)^{-1}\right]; \\ T' &= \left[y_0 + 0.5y_0^{-1}(U_1 + U_2)\mu(dP/dx)^{-1}\right]. \end{aligned} \tag{7}$$

We note that $T < T'$Also, T becomes 0 (profile 4 in Fig. 20) when

$$(U_1 + U_2)(dP/dx)^{-1} = (2y_0^2\mu^{-1}),$$

i.e., for

$$(dP/dx) = 0.5\mu y_0^{-2}(U_1 + U_2) \tag{8}$$

In this situation, from Eqs.5 and 8, the profile, independent of viscosity, is given by

$$x = 0.5(U_1 - U_2) + 0.5y_0^{-1}(U_1 + U_2) \times \left\{y - 0.5y_0^{-1}(y_0^2 - y^2)\right\} \quad (9)$$

T is <0 (profile-5 in Fig. 20)

$$\text{when } (U_1 + U_2)(\mathrm{d}P/\mathrm{d}x)^{-1} > \left(2{y_0}^2\mu^{-1}\right) \quad (10)$$

References

Annen C, Scaillet B, Sparks RSJ (2006) Thermal constraints on the emplacement rate of a large intrusive complex: the Manaslu Leucogranite, Nepal Himalaya. J Petrol 47:71–95. doi: 10.1093/petrology/egi068

Argles TW, Edwards MA (2002) First evidence of high-grade, Himalayan age synconvergent extension recognized within the western syntaxis- Nanga Parbat, Pakistan. J Struct Geol 24:1327–2344

Beaumont C, Jamieson RA, Nguyen MH et al (2001) Himalayan tectonics explained by extrusion of a low-viscosity crustal channel coupled to focused surface denudation. Nature 414:738–742

Beaumont C, Jamieson RA, Nguyen MH et al (2004) Crustal channel flows: 1. Numerical models with application to the tectonics of the Himalayan–Tibetan Orogen. J Geophys Res 109:B06406. doi:10.1029/2003JB002809

Bèrthe D, Choukroune P, Jegouzo P (1979) Orthogneiss, mylonite and non-coaxial deformation of granite: the example of the south Armorican shear zone. J Struct Geol 1:31–42

Caldwell WB, Klemperer SL, Rai SS et al (2009) Partial melt in the upper-middle crust of the northwest Himalaya revealed by Rayleigh wave dispersion. Tectonophysics (in press)

Carosi R, Musumeci G, Pertusali PC (1999) Extensional tectonics in the higher Himalayan Crystallines of Khumbu Himal, eastern Nepal. In: Macfarlane A, Sorkhabi RB, Quade J (eds) Himalaya and Tibet: mountain roots to mountain tops. Geol Soc Am Spec Publ 328, Boluder, pp 211–223

Carosi R, Montomili C, Visonà D (2007) A structural transect in the lower Dolpo: insights in the tectonic evolution of Western Nepal. J Asian Earth Sc 29:407–423

Catlos, EJ (2000) Geochronologic and Thermobarometric constraints on the evolution of the main central thrust, Himalayan Orogen. Unpublished Ph.D. Dissertation. University of California, Los Angeles. pp xix–xx

Cottle JM, Jessup MJ, Newell DL et al (2007) Structural insights into the early stages of exhumation along an orogen-scale detachment: the South Tibetan Detachment System, Dzakaa Chu section, Eastern Himalaya. J Struct Geol 29:1781–1797

Davis GH, Reynolds SJ (1996) Structural geology of rocks and regions, 2nd edn. Wiley, New York

Dèzes PJ (1999) Tectonic and Metamorphic evolution of the central Himalayan domain in southeast Zanskar (Kashmir India). Ph.D. Thesis. University of Lausanne, Switzerland. pp 1–160

Dèzes PJ, Vannay JC, Steck A et al (1999) Synorogenic extension: quantitative constraints on the age and displacement of the Zanskar shear Zone. Geol Soc Am Bull 111:364–374

Druguet E, Carreras J (2006) Analog modeling of syntectonic leucosomes in mylonitic schists. J Struct Geol 28:1734–1747

Fraser G, Worley B, Sandiford M (2000) High-precision geothermometry across the High Himalayan metamorphic sequence, Langtang Valley, Nepal. J Meta Geol 18:665–681

Fusseis F, Handy MR (2008) Micromechanisms of shear zone propagation at the brittle–viscous transition. J Struct Geol 30:1242–1253

Gansser A (1964) Geology of the Himalayas. Wiley, New York

Ghosh SK (1993) Structural geology fundamental and modern development. Pergamon, Oxford

Godin L, Brown RL, Hanmer S (1999) High strain zone in the hanging wall of the Annapurna detachment, central Nepal Himalaya. In: Macfarlane A, Sorkhabi RB, Quade J (eds) Himalaya and Tibet: mountain roots to mountain tops. Geol Soc Am Spec Pap 328: 199–210

Godin L, Grujic D, Law RD et al (2006) Channel flow, extrusion and exhumation in continental collision zones: an introduction. In: Law RD, Searle MP (eds) Channel flow, extrusion and exhumation in continental collision zones. Geol Soc London Spec Publ 268: 1–23

Grasemann B, Vanney J-C (1999) Flow controlled inverted metamorphism in shear zones. J Struct Geol 21:743–750

Grasemann B, Edwards MA, Wiesmayr G (2006) Kinematic dilatancy effects on orogenic extrusion. In: Law RD, Searle MP, Godin L (eds) Channel flow, ductile extrusion and exhumation in continental collisional zones. Geol Soc London Spec Publ 268, pp 183–199

Grujic D, Casey M, Davidson C et al (1996) Ductile extrusion of the Higher Himalayan Crystalline in Bhutan: evidence from quartz microfabrics. Tectonophys 260:21–43

Grujic D, Hollister LS, Parrish RR (2002) Himalayan metamorphic sequence as an orogenic channel: insight from Bhutan. Earth Planetary Sci Lett 198:177–191

Harris N (2007) Channel flow and the Himalayan–Tibetan orogen: a critical review. J Geol Soc Lond 164:511–523

Herren E (1987) Zanskar Shear Zone: northeast southwest extension within the Higher Himalaya (Ladakh, India). Geology 15:409–413

Hipperitt JFM (1993) 'V' pull-apart microstructures: a new shear sense indicator. J Struct Geol 15:1394–1403

Hodges KV (2000) Tectonics of the Himalaya and southern Tibet from two decades perspectives. Geol Soc Am Spec Bull 112:324–350

Hodges KV, Le Fort P, Pêcher A (1988) Possible thermal buffering by crustal anatexis in collisional orogens: Thermobarometric evidence from the Nepalese Himalaya. Geology 16:707–710

Hollister LS, Grujic D (2006) Himalaya Tiber Plateau. Pulsed channel flow in Bhutan. In: Law RD, Searle M, Godin L (eds) Channel flow, Ductile Extrusion and Exhumation in Continental Collision Zones. Geol Soc Lond Spec Publ 268, pp 415–423

Hubbard MS (1996) Ductile shear as a cause of inverted metamorphism: example from the Nepal Himalaya. J Geol 104:493–499

Inger S (1998) Timing of the extensional detachment during convergent orogeny: new Rb–Sr geochronological data from the Zanskar shear zone, northwestern Himalaya. Geology 26:223–226

Israil M, Tyagi DK, Gupta PK et al (2008) Magnetotelluric investigations for imaging electrical structure of Garhwal Himalayan corridor, Uttarakhand, India. J Earth Syst Sci 117:189–200

Jain AK, Anand A (1988) Deformational and strain patterns of an intracontinental ductile shear zone- an example from the Higher Garhwal Himalaya. J Struct Geol 10:717–734

Jain AK, Manickavasagam RM (1993) Inverted metamorphism in the intracontinental ductile shear zone during Himalayan collision tectonics. Geology 21:407–410

Jain AK, Patel RC (1999) Structure of the Higher Himalayan Crystallines along the Suru-Doda Valleys (Zanskar), NW-Himalaya. In: Jain AK, Manickavasagam RM (eds) Geodynamics of the NW Himalaya. Gond Res Gp Mem No 6. Field Science, Osaka, pp 91–110

Jain AK, Manickavasagam RM, Singh S (1999) Collision tectonics in the NW Himalaya: deformation, metamorphism and emplacement of leucogranite along Beas-Parbati Valleys, Himachal Pradesh. In: Jain AK, Manickavasagam RM (eds) Geodynamics of the NW Himalaya, Gond Res. Gp Mem. No 6. Field Science, Osaka, pp 3–37

Jain AK, Kumar D, Singh S et al (2000) Timing, quantification and tectonic modelling of Pliocene-Quaternary movements in the NW Himalaya: evidences from fission track dating. Earth Planet Sci Lett 179:437–451

Jain AK, Singh S, Manickavasagam RM (2002) Himalayan Collisional Tectonics. Gond Res Gp Mem No. 7. Field Science, Hashimoto, p 4

Jain AK, Manickavasagam RM, Singh S et al (2005) Himalayan collision zone: new perspectives- its tectonic evolution in a combined ductile shear zone and channel flow model. Him Geol 26(1):1–18

Jamieson RA, Beaumont C, Nguyen MH et al (2002) Interaction of metamorphism, deformation and extrusion in large convergent orogens. J Meta Geol 20:9–24

Jamieson RA, Beaumont C, Medvedev S et al (2004) Crustal Channel Flows: 2. Numerical models with implications for metamorphism in the Himalayan–Tibetan Orogen. J Geophys Res 109:B066407. doi:10.1029/2003JB002811

Jessel MW (1987) Grain boundary migration microstructures in naturally deformed quartzite. J Struct Geol 9:1007–1014

Kellet D A-M (2006) Characterization and age of north-verging back structures in the Tethyan Sedimentary Sequence, Hidden Valley, central Nepal Himalaya. Unpublished M.Sc. thesis. Queen's University, Canada. p 27

Kellet DA, Godin L (2009) Pre-Miocene deformation of the Himalayan superstructure, Hidden valley, central Nepal. J Geol Soc London 166:1–14

Kohn MJ (2008) P-T-t data from central Nepal support critical taper and reduplicate large-scale channel flow of the Greater Himalayan Sequence. Geol Soc Am Bull 120:259–273

Law R, Searle MP, Simpson RL (2004) Strain, deformation temperatures and vorticity of flow at the top of the Greater Himalayan Slab, Everest Massif, Tibet. J Geol Soc London 161:305–320

Manickavasagam RM, Jain AK, Singh S et al (1999) Metamorphic evolution of the northwest Himalaya, India: pressure-temperature data, inverted metamorphism, and extrusion in the Kashmir, Himachal and Garhwal Himalayas. In: Macfarlane A, Sorkhabi RB, Quade J (eds) Himalaya and Tibet Mountain Roots and Mountain Tops. Geol Soc Am Sp Pap 328:179–198

McClay KR, Insley MW (1986) Duplex structures in the lewis thrust sheet, crowsnest pass, rocky mountains, Alberta. Canada. J Struct Geol 8:911–922

Molli G, Iacopini D, Pertusati PC, Mushumeci G (Internet Reference) Architecture, strain features and fault rock types of the South Tibetan Detachment system between Katra and Tingri (South Tibet Himalaya). http://209.85.175.104/search?q=cache:DWXY1Ve5_T8J:www.see.leeds.ac.uk/peachandhorne/friday/047_Mollietal.pdf+Architecture,+strain+features+and+fault+rock+types+of+the+South+Tibetan+Detachment+system+betwe&hl=en&ct=clnk&cd=1&gl=in (Accessed on 1 May 2008)

Mukherjee S (2007) Geodynamics, deformation and mathematical analysis of metamorphic belts of the NW Himalaya. Unpublished Ph.D. thesis. Indian Institute of Technology Roorkee. pp 1–263

Mukherjee S (2008) Manifestation of brittle thrusting in micro-scale in terms of micro-duplexes of minerals in the Higher Himalayan Shear Zone, Sutlej & Zanskar section, northwest Indian Himalaya. GeoMod2008. International Geological Modelling Conference. Florence, Italy. 22–24 September. Bolletino di Geofisica Teorica e Applicata 42: 254–257

Mukherjee S (2009) Flanking Microstructures of the Zanskar Shear Zone, Western Indian Himalaya. Int J Earth Sci (submitted)

Mukherjee S, Koyi HA (2009a) Higher Himalayan Shear Zone, Sutlej section-structural geology & extrusion mechanism by various combinations of pure shear, simple shear & channel flow in shifting modes. Int J Earth Sci (in review)

Mukherjee S, Koyi HA (2009b) Flanking Microstructures. Geol Mag (in press)

Mukherjee S, Koyi HA, Talbot CJ (2009) Out-of-Sequence Thrust in the Higher Himalaya- a Review & Possible Genesis. Vol. 11, EGU2009-13783. European Geosciences Union General Assembly. Geophys Res Abs. Vienna, Austria, 19–24 April. http://meetingorganizer.copernicus.org/EGU2009/EGU2009-13783.pdf (Accessed on 10 May 2009)

Nelson KD et al (1996) Partially molten middle crust beneath Southern Tibet: synthesis of project INDEPTH results. Science 274:1684–1696

Pai S-I (1956) Viscous flow theory I-laminar flow. D. Van Nostrand, New Jersey, p 51

Passchier CW, Trouw RAJ (2005) Microtectonics, 2nd edn. Springer, Berlin, p 43

Patel RC, Singh S, Asokan A et al (1993) Extensional tectonics in the Himalayan orogen, Zanskar, NW India. In: Treloar PJ, Searle MP (eds) Himalayan Tectonics. Geol Soc London Spec Publ 74:445–459

Petit JP (1987) Criteria for the sense of movement on fault surfaces in brittle rocks. J Struct Geol 9:597–608

Ramsay JG, Lisle R (2000) The techniques of modern structural geology 3: applications of continuum mechanics in structural geology. Academic Press, San Diego, pp 837–884

Rogers RH (1978) Fluid Mechanics. Routledge & Kegan Paul, London, pp 93–109

Scaliot B, Holtz F, Pichavant M (1996) Viscosity of Himalayan Leucogranites: implications for mechanisms of granite magma ascent. J Geophys Res 101:27691–27700

Schlichting H (1955) (Translated by Kestin J) Boundary layer theory. McGraw Hill, New York, p 60

Searle MP (1999) Extensional and compressional faults in the Everest-Lhotse massif, Khumbu Himalaya. J Geol Soc London 156:227–240

Searle MP, Godin L (2003) The South Tibetan Detachment and the Manaslu Leucogranite: a structural reinterpretation and restoration of the Annapurna–Manaslu Himalaya, Nepal. J Geol 111:505–523

Searle MP, Cooper DJW, Rex AJ (1988) Collision tectonics of the Ladakh-Zanskar Himalaya. In: Shackleton RM, Dewey JF, Windley BF (eds) Tectonic evolution of the Himalayas and Tibet. Philosophical Transaction of the Royal Society, London, A326, pp 117–150

Searle MP, Waters DJ, Rex AJ et al (1992) Pressure, temperature, and time constraints on Himalayan metamorphism from eastern Kashmir and western Zanskar. J Geol Soc London 149: 753–773

Steck A, Epard J-C (2004) The Eastern prolongation of the Zanskar Shear Zone (Western Himalaya). Eclo Geol Helv 97:193–212

Stephenson BJ, Searle MP, Waters DJ et al (2001) Structure of the main Central Thrust zone and extrusion of the High Himalayan deep crustal wedge, Kishtwar-Zanskar Himalaya. J Geol Soc London 158:637–652

ten Grotenhuis SM, Passchier CW, Bons PD (2002) The influence of strain localization on the rotation behaviour of rigid objects in experimental shear zones. J Struct Geol 24:485–499

Thakur VC (1993) Geology of Western Himalaya. Pergamon, Oxford

Thiede RC, Bookhagen B, Arrowsmith JR et al (2004) Climatic control on rapid exhumation along the Southern Himalayan Front. Earth Planetary Sc Lett 222:791–806

Treagus S, Lan L (2004) Deformation of square objects and boudins. J Struct Geol 26:1361–1376

Treagus SH, Hudleston PJ, Lan L (1996) Non-ellipsoidal inclusions as geological strain markers and competence indicators. J Struct Geol 18:1167–1172

Tripathi A, Gairola VK (1999) P-T conditions of metamorphism in the Garhwal Nappe. In: Jain AK, Manickavasagam RM (eds) Geodynamics of the NW Himalaya. Gond Res Gr Mem No 6. Field Science, Osaka, pp 167–172

Valdiya KS (1998) Dynamic Himalaya. University Press, Bangalore

Valdiya KS (2001) Reactivation of terrane-defining boundary thrusts in central sectors of the Himalaya: implications. Curr Sci 81:1418–1431

Vannay J-C, Grasemann B (2001) Himalayan inverted metamorphism and syn-convergence extension as a consequence of a general shear extrusion. Geol Mag 138:253–276

Vannay JC, Grasemann B, Rahn M et al (2004) Miocene to Holocene exhumation of metamorphic crustal wedge in the NW Himalaya: evidence for tectonic extrusion coupled to fluvial erosion. Tectonics 23: TC1014: 1-24

Vernon RH (2004) A practical guide to rock microstructure. Cambridge University Press, Cambridge

Walker JD, Martin MW, Bowring SA et al (1999) Metamorphism, melting and extension: age constrains from the High Himalayan slab of southeast Zanskar and northwest Lahul. J Geol 107:473–495

Walker CB, Searle MP, Waters DJ (2001) An integrated tectonothermal model for the evolution of the High Himalaya in western Zanskar with constraints from thermobarometry and metamorphic modeling. Tectonics 20:810–833

Weinberger R, Lyakhovsky V, Baer G et al (2006) Mechanical modeling and InSAR measurements of Mount Sedom uplift, Dead Sea basin: implications for effective viscosity of rock salt. Geophys Geochem Geosys 7:Q05014. doi:10.1029/2005GC001185

Wennberg OP (1996) Superimposed fabric due to reversal of shear sense: an example from the Bergen Arc Shear Zone, western Norway. J Struct Geol 18:871–889

Wobus C, Heimsath A, Whipple K (2005) Active out-of-sequence thrust faulting in the central Nepalese Himalaya. Nature 434:1008–1011

Yin A (2006) Cenozoic tectonic evolution of the Himalayan orogen as constrained by along-strike variation of structural geometry, extrusion history, and foreland sedimentation. Earth Sci Rev 76:1–131